



HAL
open science

Emission properties of Tm³⁺-doped CaF₂, KY₃F₁₀, LiYF₄, LiLuF₄ and BaY₂F₈ crystals at 1.5 μm and 2.3 μm

Pavel Loiko, Jean-Louis Doualan, Lauren Guillemot, Richard Moncorgé, Florent Starecki, Abdelmjid Benayad, Elena Dunina, Alexey Kornienko, Liudmila Fomicheva, A. Braud, et al.

► To cite this version:

Pavel Loiko, Jean-Louis Doualan, Lauren Guillemot, Richard Moncorgé, Florent Starecki, et al.. Emission properties of Tm³⁺-doped CaF₂, KY₃F₁₀, LiYF₄, LiLuF₄ and BaY₂F₈ crystals at 1.5 μm and 2.3 μm . *Journal of Luminescence*, 2020, 225, pp.117279. 10.1016/j.jlumin.2020.117279 . hal-03060516

HAL Id: hal-03060516

<https://hal.science/hal-03060516>

Submitted on 20 May 2022

HAL is a multi-disciplinary open access archive for the deposit and dissemination of scientific research documents, whether they are published or not. The documents may come from teaching and research institutions in France or abroad, or from public or private research centers.

L'archive ouverte pluridisciplinaire **HAL**, est destinée au dépôt et à la diffusion de documents scientifiques de niveau recherche, publiés ou non, émanant des établissements d'enseignement et de recherche français ou étrangers, des laboratoires publics ou privés.



Distributed under a Creative Commons Attribution - NonCommercial 4.0 International License

Emission properties of Tm³⁺-doped CaF₂, KY₃F₁₀, LiYF₄, LiLuF₄ and BaY₂F₈ crystals at 1.5 μm and 2.3 μm

Pavel Loiko^a, Jean-Louis Doualan^a, Lauren Guillemot^a, Richard Moncorgé^a, Florent Starecki^a, Abdelmjid Benayad^a, Elena Dunina^b, Alexey Kornienko^b, Liudmila Fomicheva^c, Alain Braud^a, and Patrice Camy^{a,*}

^aCentre de recherche sur les Ions, les Matériaux et la Photonique (CIMAP), UMR 6252 CEA-CNRS-ENSICAEN, Université de Caen Normandie, 6 Boulevard du Maréchal Juin, 14050 Caen Cedex 4, France

^bVitebsk State Technological University, 72 Moskovskaya Ave., 210035 Vitebsk, Belarus

^cBelarusian State University of Informatics and Radioelectronics, 6 Brovka St., 220027 Minsk, Belarus

*Corresponding author, e-mail: patrice.camy@ensicaen.fr

Abstract. Thulium ions (Tm³⁺) are known for their emissions in the near- and mid-infrared spectral ranges suitable for efficient laser operation. We systematically study the stimulated-emission cross-sections σ_{SE} for the $^3H_4 \rightarrow ^3F_4$ (at ~1.5 μm) and $^3H_4 \rightarrow ^3H_5$ (at ~2.3 μm) Tm³⁺ transitions in five low-phonon energy fluoride single-crystals, namely, cubic Tm:CaF₂ and Tm:KY₃F₁₀, tetragonal Tm:LiYF₄ and Tm:LiLuF₄ and monoclinic Tm:BaY₂F₈. A promising material is Tm:BaY₂F₈ which offers broad and intense polarized emission spectra in the mid-infrared (2251 to 2452 nm); the maximum σ_{SE} is 0.39×10^{-20} cm² at 2289 nm (for $E \parallel Z$) and the emission bandwidth is exceeding 100 nm (for $E \parallel X$). We also revise the transition probabilities for Tm³⁺ ions in LiLuF₄ and BaY₂F₈ crystals using the Judd-Ofelt formalism and accounting for an intermediate configuration interaction (ICI).

Keywords: fluoride crystals; thulium ions; spectroscopy; stimulated-emission; Judd-Ofelt theory.

1. Introduction

Rare-earth ions (RE^{3+}) are attractive for achieving laser emission in the near and mid infrared (IR) spectral ranges. A clear example is the thulium ion (Tm^{3+}) with the electronic configuration $[\text{Xe}]4f^{12}$. The Tm^{3+} ion is known for its eye-safe emission at $\sim 1.9 \mu\text{m}$ [1] due to the transition from the lowest-lying metastable excited-state, ${}^3\text{F}_4 \rightarrow {}^3\text{H}_6$, Fig. 1. Due to the typically large Stark splitting of the ${}^3\text{H}_6$ ground-state ($\Delta E = 419 \text{ cm}^{-1}$ for $\text{Tm}:\text{LiYF}_4$ [2]), Tm^{3+} -doped materials provide broadband emissions which are favorable for wavelength-tunable [3] and ultrashort-pulse mode-locked (ML) lasers [4]. Tm^{3+} ions can be efficiently excited at $\sim 0.8 \mu\text{m}$, e.g., by commercial AlGaAs laser diodes, according to the ${}^3\text{H}_6 \rightarrow {}^3\text{H}_4$ transition [5]. The cross-relaxation (CR) process for neighboring Tm^{3+} ions, ${}^3\text{H}_4 + {}^3\text{H}_6 \rightarrow {}^3\text{F}_4 + {}^3\text{F}_4$, is efficient at moderate Tm^{3+} doping levels. It enhances the pump quantum efficiency for $\sim 1.9 \mu\text{m}$ lasers up to 2 and reduces the unwanted heat dissipation [6].

Less common but interesting for applications, transitions of Tm^{3+} ions also originate from the ${}^3\text{H}_4$ state, at $\sim 1.5 \mu\text{m}$ (${}^3\text{H}_4 \rightarrow {}^3\text{F}_4$) [7-10] and $\sim 2.3 \mu\text{m}$ (${}^3\text{H}_4 \rightarrow {}^3\text{H}_5$) [11-17], Fig. 1. The laser emission at the eye-safe wavelengths around $1.5 \mu\text{m}$ (in the near-IR) is suited for telecom, range-finding and remote sensing applications. The emission at $\sim 2.3 \mu\text{m}$ spectrally falls into the mid-IR spectral range known as a molecular fingerprint region; it is thus of practical importance for remote sensing of atmospheric species (such as CO, H_2CO or CH_4) [18,19], infrared countermeasures and non-invasive glucose ($\text{C}_6\text{H}_{12}\text{O}_6$) blood measurements [20]. $2.3 \mu\text{m}$ lasers can be also potentially used as optical pump sources of mid-IR semiconductor lasers and OPOs.

The development of $\sim 2.3 \mu\text{m}$ Tm lasers is constrained by the search of a suitable gain material. The obvious limitation is the lifetime of the ${}^3\text{H}_4$ level (energy gap to the lower-lying state: $\sim 4100 \text{ cm}^{-1}$). It can be seriously quenched by the multiphonon non-radiative (NR) relaxation, so that the low-phonon energy materials accommodating Tm^{3+} ions are preferable. Fluoride crystals appear as excellent candidates for this aim, as they (i) provide relatively low phonon energies, $400\text{-}500 \text{ cm}^{-1}$, leading to weak NR relaxations [21], (ii) have good thermal properties [22] allowing for power scaling [23], (iii) have a broad transparency range and small refractive indices [24], (iv) exhibit long emission lifetimes favorable for energy storage [25], and (v) can be generally doped with large amounts of Tm^{3+} dopants [26].

Among the fluoride laser host crystals, the most developed ones for Tm^{3+} doping are CaF_2 [27], KY_3F_{10} (both cubic) [28], LiYF_4 [29], LiLuF_4 (both tetragonal) [30] and BaY_2F_8 (monoclinic) [31]. In the present work, we limit our considerations to these crystals. Efficient lasers based on these Tm^{3+} -doped fluoride crystals operating on the ${}^3\text{F}_4 \rightarrow {}^3\text{H}_6$ transition at $\sim 1.9 \mu\text{m}$ [27-31] have been already reported. Other crystal compositions such as SrF_2 , LiGdF_4 or KYF_4 are known for Tm^{3+} -doping [32-34] while they are rarely used.

Regarding the $\sim 2.3 \mu\text{m}$ lasers based on Tm^{3+} -doped fluoride crystals, the previous studies focused mainly on the $\text{Tm}:\text{LiYF}_4$ one, which may be explained by its well-developed growth procedure by the Czochralski (Cz) method [35]. Pinto *et al.* demonstrated the first CW $\text{Tm}:\text{LiYF}_4$ laser generating 0.22 W at $2.30 \mu\text{m}$ with a slope efficiency of 15% and a continuous wavelength tunability over the $2.20\text{-}2.46 \mu\text{m}$ range [12]. Loiko *et al.* reported on

power scaling of a similar laser (up to 0.73 W at 2.306 μm) and improvement of the slope efficiency (up to 47.3%) [36]. This was referred to a positive action of energy transfer upconversion (ETU) process, ${}^3\text{F}_4 + {}^3\text{F}_4 \rightarrow {}^3\text{H}_6 + {}^3\text{H}_4$ (Fig. 1), recycling the population of the ${}^3\text{H}_4$ level at high pump intensities. Alternative pumping schemes for ~ 2.3 μm Tm:LiYF₄ lasers were proposed either relying on Yb³⁺,Tm³⁺ codoping (for pumping at ~ 0.98 μm) [8,37] or based on upconversion pumping and the photon avalanche mechanism (for pumping at ~ 1 μm or ~ 1.5 μm) [38,39].

The limited selection of fluoride laser crystals for ~ 2.3 μm Tm lasers can be attributed to the lack of spectroscopic information about transitions originating from the ${}^3\text{H}_4$ state, and, in particular, the stimulated-emission (SE) cross-sections for principal light polarizations. SE cross-sections, CR and ETU parameters of Tm:LiYF₄ crystal were recently reported [36]. Braud *et al.* analyzed the energy-transfer properties of Yb³⁺,Tm³⁺-codoped KY₃F₁₀, LiYF₄ and BaY₂F₈ for laser operation at ~ 1.5 μm and ~ 2.3 μm [9]. CW laser emission at ~ 2.3 μm was recently reported in Tm:KY₃F₁₀ however without the complete spectroscopic information around 1.5 and 2.3 μm [39,40].

In the present work, we aim to perform a comparative spectroscopic study of the main fluoride crystals intended for Tm³⁺ doping, namely, CaF₂, KY₃F₁₀, LiYF₄, LiLuF₄ and BaY₂F₈, regarding their stimulated emission (SE) properties at the ${}^3\text{H}_4 \rightarrow {}^3\text{F}_4$ and ${}^3\text{H}_4 \rightarrow {}^3\text{H}_5$ transitions, which is a prerequisite for further development of mid-infrared light sources.

2. Materials

2.1. Crystal growth

The Tm:KY₃F₁₀, Tm:LiYF₄, Tm:LiLuF₄ and Tm:BaY₂F₈ crystals were grown by the Czochralski (Cz) technique using a resistive heating furnace. The starting materials were prepared from a stoichiometric mixture of KF (or LiF, or BaF₂), YF₃ (or LuF₃) and TmF₃ powders with a 4N purity. They were thoroughly mixed and the mixtures were placed into a glassy carbon crucible. The chamber was evacuated to a pressure of 10^{-5} mbar and the crucible was heated to the temperature of 450 $^\circ\text{C}$ for 24 h to remove oxygen impurities. Then, the chamber was filled with high-purity Ar and CF₄ gases until reaching atmospheric pressure and the crucible was heated up to the melting temperature for few hours. The crystal growth was carried out using an oriented seed of a corresponding undoped crystal. The pulling rate was 1 – 3 mm/h.

In the case of Tm,Y:CaF₂, the crystal was grown by using a conventional Bridgman technique. A mixture of CaF₂, YF₃ and TmF₃ powders (purity: 4N) was placed in a graphite crucible within the growth chamber. A good vacuum ($<10^{-5}$ mbar) was then realized before introducing the Ar and CF₄ gases to reduce oxygen and water pollution. The crystal growth was carried out with a pulling rate of 3-5mm/h.

After completing the growth process, the grown crystals were cooled down to room temperature within 48 h.

For the spectroscopic studies, we used the crystals with the following composition: 1.5 at.% Tm, 4 at.% Y:CaF₂, 5.0 at.% Tm:KY₃F₁₀, 3.0 at.% Tm:LiYF₄, 9.3 at.% Tm:LiLuF₄ and 0.5 at.% Tm:BaY₂F₈. Here, the actual doping concentrations (in the crystal) are specified.

2.2. Crystal structure

The KY₃F₁₀ crystals are cubic (fluorite-type structure, sp. gr. O_h⁵ - *Fm3⁻m*). In the structure of KY₃F₁₀, there is one type of substitutional rare-earth ion site: the Y³⁺ one, with the local site symmetry C_{4v} [41]. The lattice constant of undoped KY₃F₁₀ is $a = 11.553 \text{ \AA}$.

The CaF₂ crystals possesses the same structure (sp. gr. O_h⁵ - *Fm3⁻m*) but the Tm³⁺ sites in CaF₂ are more complicated because of the charge compensation required [42]. In general, the Tm³⁺ ions replace for the Ca²⁺ cations while the charge compensation is achieved by interstitial F⁻ anions. We will consider the case of intermediate Tm³⁺ doping level (1–3 at.%) for which the majority of Tm³⁺ ions form clusters with relatively close spectroscopic properties. The introduction of optically passive Y³⁺ cations helps to prevent excessive self-quenching of the Tm³⁺ luminescence from the ³H₄ emitting state [43]. Extended discussion about ion clustering and site symmetry for Tm³⁺:CaF₂ can be found elsewhere [42]. For an undoped CaF₂, $a = 5.451 \text{ \AA}$.

The scheelite-type LiYF₄ and LiLuF₄ tetragonal crystals are isostructural (sp. gr. C_{4h}⁶ - *I4₁/a*). They exhibit a single substitutional rare-earth ion site (Y³⁺ and Lu³⁺, respectively, the local site symmetry is S₄) [26]. The lattice constants for undoped crystals $a = b = 5.164 \text{ \AA}$, $c = 10.741 \text{ \AA}$ (for LiYF₄) and $a = b = 5.146 \text{ \AA}$, $c = 10.589 \text{ \AA}$ (for LiLuF₄).

Finally, BaY₂F₈ belongs to the monoclinic crystal class (sp. gr. C_{2h}³ - *C2/m*) [44]. It also has a single rare-earth ion site (the Y³⁺ one with the C₂ local site symmetry). The C₂ symmetry axis is parallel to the **b** crystallographic axis which determines the anisotropy of the physical properties. The lattice constants are $a = 6.983 \text{ \AA}$, $b = 10.519 \text{ \AA}$, $c = 4.264 \text{ \AA}$ and the monoclinic angle is $\beta = a^{\wedge}c = 99.7^{\circ}$.

The Tm³⁺ ion density N_{Tm} corresponding to a 1 at.% doping level for the studied crystals is listed in Table 1.

In Table 1, we also list the maximum phonon frequency $h\nu_{\text{ph}}$, ranging from 420 cm⁻¹ for BaY₂F₈ to ~495 cm⁻¹ for CaF₂ and KY₃F₁₀. According to the “energy gap law”, which stipulates that the multiphonon NR relaxation is weak when the number of phonons needed to bridge the energy gap to the lower-lying multiplet is over 4 [45], the NR relaxation from the ³H₄ emitting state down to the next underlying ³H₅ multiplet of the Tm³⁺ ions (of the order of 4000 cm⁻¹ [2]) in the studied fluoride crystals should be nearly negligible.

2.3. Optical orientation of samples

The CaF₂ and KY₃F₁₀ crystals are optically isotropic. For CaF₂, the dispersion curve was reported yielding $n = 1.422$ at ~2.3 μm [24] and for KY₃F₁₀, only a mean refractive index value $\langle n \rangle \approx 1.47$ is known.

Both LiYF₄ and LiLuF₄ are optically uniaxial. The optical axis (O.A.) is parallel to the crystallographic **c**-axis, so that there are two principal light polarizations, $\mathbf{E} \parallel \mathbf{c}$ (π) and $\mathbf{E} \perp \mathbf{c}$ (σ) with the corresponding refractive indices n_e and n_o , Fig. 2(a). For these crystals, $n_e > n_o$ (positive uniaxial crystals). According to the dispersion curves of LiYF₄ [46], $n_o = 1.440$ and $n_e = 1.463$ at ~2.3 μm.

The BaY₂F₈ crystal is optically biaxial. Its optical properties are then described in the frame of the optical indicatrix with three orthogonal axes, (X, Y, Z), Fig. 2(b). One of them is parallel to the C₂ symmetry axis (Y || **b**-axis) and the other two are lying in the **a-c** plane. The Z-axis can be found by 21° anti-clockwise rotation from the **c**-axis (in the monoclinic angle, for **b**-axis pointing towards the observer), and the angle X[^]**a** = 11.3°. Typically for monoclinic laser crystals, the optical indicatrix axes (X, Y, Z) are also labeled as (N_p, N_m, N_g) (a note: not necessarily respectively) according to the relation between the principal refractive indices: n_p < n_m < n_g. However, in the literature, there exists some confusion in such assignment for BaY₂F₈ (for example, an exchange of the X and Z axes). In the present work, we follow the notations used in Ref. [47]. Using the dispersion data by Kaminskii *et al.*, we calculated n_x = 1.466, n_y = 1.522 and n_z = 1.502 at ~2.3 μm [48]. Thus, we will simply refer to the **E** || X, Y and Z light polarizations.

3. Experimental

All the measurements were performed at room temperature (RT, 293 K).

The absorption spectra were measured using a spectrophotometer (Lambda 1050, Perkin Elmer) equipped with a Glan-Taylor polarizer. The spectral bandwidth (SBW) was down to 0.1 nm.

The luminescence spectra $W(\lambda)$ at 1.3–1.6 μm (³H₄ → ³F₄ emission transition) were measured using an optical spectrum analyzer (AQ6375B, Yokogawa, SBW = 1 nm). The $W(\lambda)$ spectra at 2.1–2.7 μm (³H₄ → ³H₅ emission transition) were measured using a 0.6 m monochromator (HRS2, Jobin-Yvon), a lock-in amplifier (SR810 DSP, Stanford Research Systems) and an InSb photodetector (J10D series, Judson Infrared) cooled by liquid nitrogen (SBW = 4.5 nm). A Glan-Taylor prism was used for polarized measurements. As an excitation source, we employed a CW Ti:Sapphire laser (3900S, Spectra Physics) tuned to the maximum absorption at the ³H₆ → ³H₄ transition. The wavelength calibration was performed using an Hg lamp (Schwabe). The apparatus function of the set-up $X(\lambda)$ was determined using a 20 W quartz iodine lamp providing a luminescence spectrum close to that for a black-body source. The calibrated luminescence spectra were calculated as $W_i'(\lambda) = W_i(\lambda)/X(\lambda)$, where *i* indicates the light polarization.

4. Results and discussion

4.1. Absorption cross-sections

The absorption cross-sections, σ_{abs} , were calculated from the measured absorption coefficients as $\sigma_{\text{abs}} = \alpha_{\text{abs}}/N_{\text{Tm}}$ where N_{Tm} is the Tm³⁺ ion concentration.

The absorption cross-section spectra for the ³H₆ → ³H₄ pump transition of Tm³⁺ ions are shown in Fig. 3 for the studied crystals. The wavelengths of the most intense absorption peak λ_{abs} , the corresponding peak σ_{abs} values and the peak bandwidth calculated as full width at half maximum $\Delta\lambda_{\text{abs}}$ (FWHM) are listed in Table 2.

The studied fluoride crystals exhibit very similar σ_{abs} values. The birefringent crystals show a notable anisotropy of absorption in polarized light. The preferable light polarizations

are π (for Tm:LiYF₄ and Tm:LiLuF₄) and $E \parallel Y$ (for Tm:BaY₂F₈). For example, for the latter material, $\sigma_{\text{abs}} = 0.90 \times 10^{-20} \text{ cm}^2$ at 789.3 nm with $\Delta\lambda_{\text{abs}} = 2.1 \text{ nm}$ (for $E \parallel Y$).

4.2. Stimulated-emission cross-sections

The SE cross-sections for the ${}^3\text{H}_4 \rightarrow {}^3\text{F}_4$ and ${}^3\text{H}_4 \rightarrow {}^3\text{H}_5$ transitions were calculated using the Fuchtbauer-Ladenburg (FL) formula [49]:

$$\sigma_{\text{SE}}^j(\lambda) = \frac{\lambda^5}{8\pi \langle n \rangle^2 \tau_{\text{rad}} c} \frac{W'_i(\lambda) B(JJ')}{1/3 \sum_i \int \lambda W'_i(\lambda) d\lambda}, \quad (1)$$

where λ is the light wavelength, $\langle n \rangle$ is the polarization-averaged refractive index at a mean emission wavelength $\langle \lambda_{\text{lum}} \rangle$, c is the speed of light, τ_{rad} is the radiative lifetime of the ${}^3\text{H}_4$ emitting state, $W'_i(\lambda)$ is the luminescence spectrum calibrated for the spectral response of the set-up, $B(JJ')$ is the luminescence branching ratio (assuming purely radiative transitions) for the transitions in emission between the states with the total angular momentum quantum numbers J and J' ($J = 4$ for ${}^3\text{H}_4$ and $J' = 4$ and 5 for ${}^3\text{F}_4$ and ${}^3\text{H}_5$, respectively), and i indicates the light polarization. The polarization-averaging (the factor of $1/3$) is not performed for isotropic crystals (CaF₂ and KY₃F₁₀). For optically uniaxial crystals (LiYF₄, LiLuF₄), it is performed as $(2\int_{\sigma} + \int_{\pi})/3$ and for the optically biaxial crystal (BaY₂F₈), it is $(\int_X + \int_Y + \int_Z)/3$.

In Table 3, we summarize the radiative lifetimes τ_{rad} and the luminescence branching ratios $B(JJ')$ which were used in the present work. For Tm:CaF₂, Tm:KY₃F₁₀ and Tm:LiYF₄, there exist reliable literature data on these parameters derived by means of the Judd-Ofelt (J-O) theory [41,50,51]. For Tm:LiLuF₄ and Tm:BaY₂F₈, the present literature data are not satisfactory. For Tm:BaY₂F₈, Owen *et al.* used a ‘‘mixed’’ crystal, Tm:Ba(Y,Yb)₂F₈, and did not account for the dispersion of the refractive index [47]. For Tm:LiLuF₄, Xiong *et al.* used unpolarized absorption spectra for calculations [52] while Cornacchia *et al.* provided the luminescence branching ratios with a high error [53]. Thus, for the latter materials, we performed such calculations in the present work (Section 4.3).

The results on the SE cross-sections for the ${}^3\text{H}_4 \rightarrow {}^3\text{F}_4$ transition at $\sim 1.5 \mu\text{m}$ are shown in Fig. 4. The peak emission wavelengths (λ_{em}) and the corresponding σ_{SE} values are listed in Table 4. Among the studied cubic crystals, Tm:KY₃F₁₀ provides the highest SE cross-section, $\sigma_{\text{SE}} = 0.62 \times 10^{-20} \text{ cm}^2$ at 1462 nm. The emission properties of the tetragonal Tm:LiYF₄ and Tm:LiLuF₄ crystals are very close (the cross-sections for the former one are slightly higher). These materials exhibit a remarkable polarization-anisotropy of SE cross-sections with higher σ_{SE} values in π -polarization, namely $1.14 \times 10^{-20} \text{ cm}^2$ at 1452 nm (for Tm:LiYF₄). The ratio $\sigma_{\text{SE}}(\pi) : \sigma_{\text{SE}}(\sigma)$ for this crystal is as high as 3.7. Finally, the monoclinic crystal Tm:BaY₂F₈ also exhibits some polarization-anisotropy in the σ_{SE} spectra which is however less pronounced. The highest value is observed for light polarization $E \parallel Y$ ($\sigma_{\text{SE}} = 0.73 \times 10^{-20} \text{ cm}^2$ at 1478 nm), and for other polarizations, a relation $\sigma_{\text{SE}}(Y) > \sigma_{\text{SE}}(Z) > \sigma_{\text{SE}}(X)$ is observed. Note that the peak emission wavelength is the same for $E \parallel X$ and Z but is different for $E \parallel Y$. This difference originates from the fact that the Y optical indicatrix axis is parallel to the b -axis (C_2 symmetry axis), and the other two axes (X and Z) are lying in the orthogonal plane. Thus, the polarization selection rules are different in these cases.

For Tm^{3+} ions, there is a strong ${}^3\text{F}_4 \rightarrow {}^3\text{H}_4$ excited-state absorption (ESA) transition (cf. Fig. 1) which spectrally overlaps with the emission at $\sim 1.5 \mu\text{m}$ [38,39]. As the ${}^3\text{F}_4$ multiplet is a metastable level, the probability of such ESA is very high. It should be considered when predicting the possible laser wavelengths for Tm laser operating on this ${}^3\text{H}_4 \rightarrow {}^3\text{F}_4$ emission transition.

Now let us discuss the results on the SE cross-sections for the ${}^3\text{H}_4 \rightarrow {}^3\text{H}_5$ transition around $2.3 \mu\text{m}$, cf. Fig. 5 and Table 4. Such a ${}^3\text{H}_4 \rightarrow {}^3\text{H}_5$ emission transition corresponds to a quasi-four level laser scheme and does not overlap with any strong ESA channel. Thus, the local peaks in the σ_{SE} spectra will determine the expected laser wavelengths and the possible emission bandwidths for ML operation [16,17].

Both cubic $\text{Tm:KY}_3\text{F}_{10}$ and Tm,Y:CaF_2 crystals exhibit broad and smooth SE cross-section spectra. For the former material, $\sigma_{\text{SE}} = 0.34 \times 10^{-20} \text{ cm}^2$ at 2342 nm with an emission bandwidth (defined as FWHM) $\Delta\lambda_{\text{em}} = 62 \text{ nm}$. For the Tm,Y:CaF_2 crystal, the peak value is smaller, $0.15 \times 10^{-20} \text{ cm}^2$ at 2372 nm, while the emission band is extremely broad ($\Delta\lambda_{\text{em}} = 252 \text{ nm}$), indicating a glassy-like spectroscopic behavior.

For the tetragonal Tm:LiYF_4 and Tm:LiLuF_4 crystals, the shape of the SE cross-section spectra is similar while slightly higher σ_{SE} values are again determined for the former material, namely $0.44 \times 10^{-20} \text{ cm}^2$ at 2304 nm with $\Delta\lambda_{\text{em}} = 34 \text{ nm}$ (for π -polarization). Similarly to the ${}^3\text{H}_4 \rightarrow {}^3\text{F}_4$ transition, an anisotropy of the SE properties is detected, however with a smaller ratio $\sigma_{\text{SE}}(\pi) : \sigma_{\text{SE}}(\sigma)$ of 1.9. This is nevertheless enough to determine a linearly polarized output in *a*-cut Tm:LiYF_4 lasers [36].

For monoclinic $\text{Tm:BaY}_2\text{F}_8$ crystal, the highest SE cross-section is observed for light polarization $\mathbf{E} \parallel \mathbf{Z}$, namely $0.39 \times 10^{-20} \text{ cm}^2$ at 2289 nm with $\Delta\lambda_{\text{em}} = 29 \text{ nm}$. For the other polarizations, a relation $\sigma_{\text{SE}}(\mathbf{Z}) > \sigma_{\text{SE}}(\mathbf{X}) > \sigma_{\text{SE}}(\mathbf{Y})$ is observed. Much broader emission bandwidths are detected for $\mathbf{E} \parallel \mathbf{Y}$ ($\Delta\lambda_{\text{em}} = 86 \text{ nm}$) and especially for $\mathbf{E} \parallel \mathbf{X}$ ($\Delta\lambda_{\text{em}} = 144 \text{ nm}$). Note that despite a relatively weak anisotropy in the peak σ_{SE} values, $\text{Tm:BaY}_2\text{F}_8$ offers several intense emission peaks at different wavelengths ranging from 2251 to 2452 nm.

All the studied Tm^{3+} -doped fluoride crystals exhibit relatively high SE cross-sections on the ${}^3\text{H}_4 \rightarrow {}^3\text{H}_5$ transition. The features of $\text{Tm:KY}_3\text{F}_{10}$ are a combination of a moderate σ_{SE} value with a broad emission bandwidth making it very suitable for broadly tunable and ML oscillators. Tm:LiYF_4 offers a high peak σ_{SE} value in π -polarization whilst corresponding to a narrower emission band. $\text{Tm:BaY}_2\text{F}_8$ features multiple broad emission peaks up to $\sim 2.45 \mu\text{m}$; it is thus attractive for going further into the mid-IR.

4.3. Judd-Ofelt modeling: Tm:LiLuF_4 and $\text{Tm:BaY}_2\text{F}_8$

As pointed out above, there is a lack of reliable data on transition probabilities of Tm^{3+} ions in LiLuF_4 and BaY_2F_8 crystals. In the present work, we performed such calculations based on measured absorption spectra for principal light polarizations (π and σ for Tm:LiLuF_4 and $\mathbf{E} \parallel \mathbf{X}, \mathbf{Y}, \mathbf{Z}$ for $\text{Tm:BaY}_2\text{F}_8$). The spectra are displayed in Fig. 6.

The transition probabilities of Tm^{3+} ions were calculated within the standard Judd-Ofelt (J-O) theory [54,55] and its modifications accounting for configuration interaction: the so-called modified Judd-Ofelt theory (mJ-O) and the approximation of an intermediate

configuration interaction (ICI) [56-58]. The J–O formalism was applied to electric-dipole (ED) contributions to the transition intensities. The contribution of magnetic-dipole (MD) transitions (following the selection rule $\Delta J = J - J' = 0, \pm 1$, except $J = J' = 0$) to the transition intensities was calculated separately within the Russell–Saunders approximation on wave functions of Tm^{3+} under an assumption of a free-ion.

A detailed description of such calculations can be found elsewhere [25,59]. Here, we only discuss the different approximations used.

For the standard J-O theory, the ED line strengths of the $J \rightarrow J'$ transitions $S^{\text{ED}}(JJ')$ are [54,55]:

$$S_{\text{calc}}^{\text{ED}}(JJ') = \sum_{k=2,4,6} U^{(k)} \Omega_k, \quad (2a)$$

$$U^{(k)} = \langle (4f^n)SLJ \| U^{(k)} \| (4f^n)S'L'J' \rangle^2. \quad (2b)$$

Here, the $U^{(k)}$ are reduced squared matrix elements calculated using the crystal-field parameters from Ref. [60] and Ω_k are the intensity (J–O) parameters (for both, $k = 2, 4, 6$).

For the ICI approximation, the ED line strengths are given by [56,58]:

$$S_{\text{calc}}^{\text{ED}}(JJ') = \sum_{k=2,4,6} U^{(k)} \Omega_k^*, \quad (3a)$$

$$\Omega_k^* = \Omega_k [1 + 2R_k(E_J + E_{J'} - 2E_f^0)]. \quad (3b)$$

Here, the intensity parameters Ω_k^* are the linear functions of energies (E_J and $E_{J'}$) of the two multiplets participating in the transition $J \rightarrow J'$, E_f^0 is the mean energy of the $4f^n$ configuration and R_k ($k = 2, 4, 6$) are the parameters representing the configuration interaction. Therefore, in the ICI approximation, there are six free parameters, namely Ω_k and R_k ($k = 2, 4, 6$) and the derived Ω_k^* will be different from those found by using Eq. (2).

If solely the lower-energy excited configuration with the opposite parity ($4f^{n-1}5d^1 = 4f^{11}5d^1$ for Tm^{3+} ions) is considered to contribute to the configuration interaction, then it is possible to write $R_2 = R_4 = R_6 = \alpha \approx 1/(2\Delta)$ where $\Delta \approx E(4f^{n-1}5d^1) - E(4f^n)$ is the average energy difference between the fundamental ($4f^{12}$) and the first-excited ($4f^{11}5d^1$) electronic configurations [56]. In that case, the expression for the ED transition intensities is simplified [56,57]:

$$S_{\text{calc}}^{\text{ED}}(JJ') = \sum_{k=2,4,6} U^{(k)} \Omega_k^*, \quad (4a)$$

$$\Omega_k^* = \Omega_k [1 + 2\alpha(E_J + E_{J'} - 2E_f^0)]. \quad (4b)$$

Now, there are four free (new) parameters, namely Ω_2 , Ω_4 , Ω_6 and α . Note that Eq. (4) for the mJ-O theory is transformed into Eq. (2) for the standard one under the assumption of a high-lying $4f^{n-1}5d^1$ excited configuration (i.e., for $\Delta \rightarrow \infty$, thus $\alpha \rightarrow 0$).

Note that the Δ parameter can be estimated from the experimental spectroscopic data and compared to the value which is obtained from the calculations within the mJ-O theory. This was performed in [56] in the case of Pr^{3+} in $\text{KPrP}_4\text{O}_{12}$. As for the fluorides, there is an extensive literature on the subject including theory and experiments [61]. According to these works, the lower-lying energy levels of the $4f^{11}5d^1$ excited electronic configuration of Tm^{3+} giving rise to the strongest $4f - 4f5d$ ED allowed absorption transitions would be located (by

using Eq. (1) from Ref. [61]) at ~160 nm for all the studied crystals, thus at about the same energy of ~62500 cm⁻¹. Assuming the 4f¹² electronic configuration with an average energy of ~10000 cm⁻¹, it means that it is expected to find a Δ value of the order of 52500 cm⁻¹ ($\alpha \approx 1/(2\Delta) = 2 \times 10^{-5}$ cm).

For both Tm:LiLuF₄ and Tm:BaY₂F₈ crystals, all the calculations were performed by averaging the polarizations, namely $\langle P \rangle = (1/3)(2P_\sigma + P_\pi)$ for the uniaxial Tm:LiLuF₄ crystal and $\langle P \rangle = (1/3)(P_X + P_Y + P_Z)$ for the biaxial Tm:BaY₂F₈ one, where P is the parameter and the subscripts indicate the polarization state.

The measured and calculated absorption oscillator strengths (denoted as $\langle f_{\text{exp}}^\Sigma \rangle$ and $\langle f_{\text{calc}}^\Sigma \rangle$, respectively) are presented in Table 5 (for Tm:LiLuF₄) and Table 6 (for Tm:BaY₂F₈). Here, the superscript “ Σ ” stands for the total (ED + MD) value.

A comparison of the root-mean-square deviations (r.m.s. dev.) between $\langle f_{\text{exp}}^\Sigma \rangle$ and $\langle f_{\text{calc}}^\Sigma \rangle$ indicates that the ICI approximation gives a better agreement between the experimental and calculated values for both crystals. For example, the r.m.s. dev. equals to 0.126 (ICI) and 0.202 (J-O) for the case of Tm:LiLuF₄. Moreover, a closer agreement is observed for the absorption oscillator strength for the transition to the first excited state (³F₄). Its value has a direct consequence on the calculated radiative lifetime of this level. Indeed, for Tm:LiLuF₄, $\langle f_{\text{exp}}^\Sigma \rangle \times 10^6 = 1.436$ while $\langle f_{\text{calc}}^\Sigma \rangle \times 10^6 = 1.375$ (ICI) and 1.588 (J-O). Thus, it is expected that the use of the standard J-O approach will underestimate the lifetime of the Tm³⁺ lower-lying excited state while this problem can be avoided when using the ICI approximation. From these considerations, we selected the latter model for further calculations.

The determined intensity parameters giving the minimum r.m.s. dev. (namely, $\{\Omega_k\}$ for the standard J-O theory, $\{\Omega_k$ and $\alpha\}$ for the mJ-O one and $\{\Omega_k$ and $R_k\}$ for the ICI approximation) are listed in Table 7.

The α values which result from the fitting procedure within the framework of the ICI approximation are of the order of 1×10^{-5} for Tm:LiLuF₄, which is very close to the above estimated value, and 1×10^{-4} for Tm:BaY₂F₈, which means that another mechanism (different from a simple configuration interaction one) could contribute.

Using the set of the intensity parameters determined within the framework of the ICI approximation, we calculated the radiative spontaneous emissions probabilities A_{calc}^Σ (here, the superscript “ Σ ” also stands for the total (ED + MD) value), the luminescence branching ratios $B(JJ')$, the total probability of radiative spontaneous transitions from an excited-state A_{tot} and the radiative lifetime of an excited state τ_{rad} . The summary of results obtained within the ICI approximation is shown in Table 8 (for Tm:LiLuF₄) and Table 9 (for Tm:BaY₂F₈).

For Tm:LiLuF₄, the radiative lifetimes of the excited-states of interest for Tm³⁺ laser operation are $\tau_{\text{rad}} = 10.99$ ms (³F₄) and 1.34 ms (³H₄). The luminescence branching ratios for the transitions of interest are $B(JJ') = 8.9\%$ (³H₄ → ³F₄) and 2.2% (³H₄ → ³H₅). These values correspond to the ICI approximation.

For Tm:BaY₂F₈, slightly shorter radiative lifetimes are determined, namely $\tau_{\text{rad}} = 8.68$ ms (³F₄) and 1.10 ms (³H₄) while the luminescence branching ratios are similar (compared to Tm:LiLuF₄), $B(JJ') = 8.8\%$ (³H₄ → ³F₄) and 3.1% (³H₄ → ³H₅).

Note that the use of a certain approximation in the J–O calculations has a minor effect on the determined luminescence branching ratios $B(JJ')$. Indeed, for the ${}^3\text{H}_4 \rightarrow {}^3\text{H}_5$ transition, $B(JJ') = 2.65\%$ (J–O), 2.57% (mJ–O) and 2.16% (ICI) for the case of Tm:LiLuF₄.

4.4. Analysis of the results

Let us examine the consistency of the determined σ_{SE} spectra for the ${}^3\text{H}_4 \rightarrow {}^3\text{F}_4$ and ${}^3\text{H}_4 \rightarrow {}^3\text{H}_5$ transitions. For this, a comparison is made between (i) the integrated σ_{abs} values derived from the transformed σ_{SE} spectra via the reciprocity method and (ii) the integrated σ_{abs} values calculated from the respective line strengths of the transitions. Note that both of the considered transitions can be of ED and MD nature. The transitions in absorption (from the ${}^3\text{F}_4$ and ${}^3\text{H}_5$ states) correspond to ESA.

For crystals with a well-defined scheme of Stark levels, the absorption cross-section of a transition between two multiplets is related to the SE cross-section of the reverse transition by the Einstein “reciprocity” expression [1]:

$$\sigma_{\text{abs}}^i(\lambda) = \sigma_{\text{SE}}^i(\lambda) \cdot \frac{Z_u}{Z_l} \cdot \exp\left[\frac{(hc/\lambda) - E_{\text{ZL}}}{kT}\right], \quad (5)$$

where h is the Planck constant, k is the Boltzmann constant, T is the crystal temperature (RT, in our case), $E_{\text{ZL}} = (hc)/\lambda_{\text{ZL}}$ is the energy of the zero line (ZL) transition between the lowest Stark sub-levels of both multiplets, and i indicates the light polarization. Z_m are the partition functions for the lower ($m = l$) and upper ($m = u$) manifolds:

$$Z_m = \sum_k g_k^m \exp(-E_k^m/kT). \quad (6)$$

Here, g_k^m is the degeneracy of the sub-level with the number k and energy E_k^m measured from the lowest sub-level of each multiplet.

From the determined absorption (ESA) cross-sections, we calculate the polarization-averaged integrated σ_{abs} values, $\int \langle \sigma_{\text{abs}} \rangle (\lambda) d\lambda$. The averaging is performed as explained in Section 4.3. Those are compared with the values determined from the line strengths [62]:

$$\int \sigma_{\text{abs}}^{\text{calc}}(\lambda) d\lambda = \frac{2\pi^2 q^2 \langle \lambda \rangle}{3hc(2J_l + 1)\epsilon_0} \left[\frac{(\langle n \rangle^2 + 2)^2}{9\langle n \rangle} S_{\text{calc}}^{\text{ED}} + \langle n \rangle S_{\text{calc}}^{\text{MD}} \right]. \quad (7)$$

Here, q is the electron charge, $\langle \lambda \rangle$ is the mean wavelength in absorption, J_l is the total angular momentum quantum number for the lower-lying ($m = l$) multiplet, ϵ_0 is the vacuum permittivity. The J–O parameters Ω_k for Tm:KY₃F₁₀ and Tm:LiYF₄ [41,49] used to calculate the $S_{\text{calc}}^{\text{ED}}$ contributions to the line strength of transitions are listed in Table 3. For Tm:LiLuF₄ and Tm:BaY₂F₈, these values were obtained within the ICI approximation using the intensity parameters from Table 7.

Due to the availability of data on the crystal-field splitting for Tm³⁺ ions [2,41,47,63], the analysis is performed for the Tm:KY₃F₁₀, Tm:LiYF₄, Tm:LiLuF₄ and Tm:BaY₂F₈ crystals. The results on the integrated σ_{abs} values obtained by using two approaches, as well as the $S_{\text{calc}}^{\text{ED}}$ and $S_{\text{calc}}^{\text{MD}}$ values are listed in Table 10. The agreement between the semi-experimental and theoretical integrated absorption cross sections is quite good. This proves the good choice

of the absorption and emission wavelengths made in the J–O treatment and of the derived intensity parameters, radiative lifetimes and branching ratios.

5. Conclusion

All the studied fluoride crystals exhibit intense and broad emission bands in the near-IR ($\sim 1.5 \mu\text{m}$) and mid-IR ($\sim 2.3 \mu\text{m}$) corresponding to the ${}^3\text{H}_4 \rightarrow {}^3\text{F}_4$ and ${}^3\text{H}_4 \rightarrow {}^3\text{H}_5$ optical transitions, respectively, originating from the same emitting state. The main interest lies in the latter emission which was recently used in a number of continuous-wave and ultrashort-pulse oscillators. So far, only two fluoride crystals have been employed for $\sim 2.3 \mu\text{m}$ lasers, namely Tm:LiYF₄ and Tm:KY₃F₁₀. The variety of the studied fluoride crystals may allow to address specific requirements for $\sim 2.3 \mu\text{m}$ lasers, such as (i) broad emission bandwidths (by using Tm:KY₃F₁₀ and Tm:CaF₂) which is of interest for broadly tunable and ML lasers, (ii) high stimulated-emission cross-sections in polarized light (by using Tm:LiYF₄, Tm:LiLuF₄ or Tm:BaY₂F₈) or (iii) long emission wavelengths extending beyond $2.4 \mu\text{m}$ (with Tm:BaY₂F₈ and combination of crystal orientation and light polarization). Note that all these crystals exhibit rather similar absorption at $\sim 0.8 \mu\text{m}$ and are suitable for efficient diode-pumping.

For the actual design of the $\sim 2.3 \mu\text{m}$ lasers, there exist other relevant spectroscopic parameters which need further studies, such as the concentration-dependent rate of the CR energy transfer (${}^3\text{H}_4 + {}^3\text{H}_6 \rightarrow {}^3\text{F}_4 + {}^3\text{F}_4$) which quenches the upper laser level lifetime, the rate of ETU depopulating the ${}^3\text{F}_4$ metastable level (${}^3\text{F}_4 + {}^3\text{F}_4 \rightarrow {}^3\text{H}_6 + {}^3\text{H}_4$) and acting as a refilling mechanism for the upper laser level, and, the ESA cross sections at $\sim 1 \mu\text{m}$ and $\sim 1.5 \mu\text{m}$ to further explore the recently proposed upconversion pumping scheme.

Separately, one should also comment on the suitability of Tm:CaF₂ for laser operation at $\sim 2.3 \mu\text{m}$. Just at a glance, this crystal is attractive because of its ultra-broadband emission properties (emission bandwidth of 252 nm, centered at 2372 nm) which are compatible with those for the Cr²⁺-doped zinc chalcogenides. However, the relatively low SE cross-section and, even more important, the extremely strong clustering of the RE³⁺ dopant ions may be a serious limitation for achieving laser operation. More dedicated study of Tm:CaF₂ is required in this regard, focusing on the possible positive role of buffer (optically passive) ions.

Acknowledgements

This work was supported by French Agence Nationale de la Recherche (ANR) through the projects LabEx EMC3 (ANR-10-LABX-09-01), SPLENDID2 (ANR-19-CE08-0028), and the European project "NOVAMAT" co-funded by the European Community funds FEDER and the Normandie region.

References

1. S.A. Payne, L.L. Chase, L.K. Smith, W.L. Kway, W.F. Krupke, Infrared cross-section measurements for crystals doped with Er³⁺, Tm³⁺, and Ho³⁺, IEEE J. Quantum Electron. 28 (1992) 2619-2630.
2. H. P. Jenssen, A. Linz, R. P. Leavitt, C. A. Morrison, D. E. Wortman, Analysis of the optical spectrum of Tm³⁺ in LiYF₄, Phys. Rev. B 11 (1975) 92-101.

3. R. C. Stoneman, L. Esterowitz, Efficient, broadly tunable, laser-pumped Tm:YAG and Tm:YSGG cw lasers, *Opt. Lett.* 15 (1990) 486–488.
4. Y. Wang, W. Chen, M. Mero, L. Zhang, H. Lin, Z. Lin, G. Zhang, F. Rotermund, Y.J. Cho, P. Loiko, X. Mateos, U. Griebner, V. Petrov, Sub-100 fs Tm:MgWO₄ laser at 2017 nm mode locked by a graphene saturable absorber, *Opt. Lett.* 42 (2017) 3076-3079.
5. E.C. Honea, R.J. Beach, S.B. Sutton, J.A. Speth, S.C. Mitchell, J.A. Skidmore, M.A. Emanuel, S.A. Payne, 115-W Tm:YAG diode-pumped solid-state laser, *IEEE J. Quantum Electron.* 33 (1997) 1592-1600.
6. K. van Dalfsen, S. Aravazhi, C. Grivas, S. M. García-Blanco, M. Pollnau, Thulium channel waveguide laser with 1.6 W of output power and ~80% slope efficiency, *Opt. Lett.* 39 (2014) 4380-4383.
7. R.C. Stoneman, L. Esterowitz, Continuous-wave 1.50 μm thulium cascade laser, *Opt. Lett.* 16 (1991) 232-234.
8. A. Dening, P.E.A. Mobert, G. Huber, Diode-pumped continuous-wave, quasi-continuous-wave and Q-switched laser operation of Yb³⁺, Tm³⁺:YLiF₄ at 1.5 and 2.3 μm, *J. Appl. Phys.* 84 (1998) 5900-5904.
9. A. Braud, S. Girard, J. L. Doualan, M. Thuau, R. Moncorgé, Energy-transfer processes in Yb:Tm-doped KY₃F₁₀, LiYF₄, and BaY₂F₈ single crystals for laser operation at 1.5 and 2.3 μm, *Phys. Rev. B* 61 (2000) 5280-5292.
10. G. Androz, M. Bernier, D. Faucher, R. Vallée, 2.3 W single transverse mode thulium-doped ZBLAN fiber laser at 1480 nm, *Opt. Express* 16 (2008) 16019-16031.
11. R. Allen, L. Esterowitz, CW diode pumped 2.3 μm fiber laser, *Appl. Phys. Lett.* 55 (1989) 721-722.
12. J.F. Pinto, L. Esterowitz, G.H. Rosenblatt, Tm³⁺:YLF laser continuously tunable between 2.20 and 2.46 μm, *Opt. Lett.* 19 (1994) 883–885.
13. L. Guillemot, P. Loiko, E. Kifle, J.L. Doualan, A. Braud, F. Starecki, T. Georges, J. Rouvillain, A. Hideur, P. Camy, Watt-level mid-infrared continuous-wave Tm:YAG laser operating on the ³H₄ → ³H₅ transition, *Opt. Mater.* 101 (2020) 109745-1-8.
14. L. Guillemot, P. Loiko, A. Braud, J.-L. Doualan, A. Hideur, M. Koselja, R. Moncorgé, P. Camy, Continuous-wave Tm:YAlO₃ laser at ~2.3 μm, *Opt. Lett.* 44 (2019) 5077-5080.
15. J. Caird, L. DeShazer, J. Nella, Characteristics of room-temperature 2.3-μm laser emission from Tm³⁺ in YAG and YAlO₃, *IEEE J. Quantum Electron.* 11 (1975) 874-881.
16. R. Soulard, A. Tyazhev, J.-L. Doualan, A. Braud, A. Hideur, M. Laroche, B. Xu, P. Camy, 2.3 μm Tm³⁺:YLF mode-locked laser, *Opt. Lett.* 42 (2017) 3534–3536.
17. F. Canbaz, I. Yorulmaz, and A. Sennaroglu, Kerr-lens mode-locked 2.3-μm Tm³⁺:YLF laser as a source of femtosecond pulses in the mid-infrared, *Opt. Lett.* 42 (2017) 3964-3967.
18. J. Wang, M. Maiorov, J. B. Jeffries, D. Z. Garbuzov, J. C. Connolly, R.K. Hanson, A potential remote sensor of CO in vehicle exhausts using 2.3 μm diode lasers, *Meas. Sci. Technol.* 11 (2000) 1576-1584.
19. F. J. McAleavey, J. O’Gorman, J. F. Donegan, B. D. MacCraith, J. Hegarty, G. Maze, Narrow linewidth, tunable Tm³⁺-doped fluoride fiber laser for optical-based hydrocarbon gas sensing, *IEEE J. Sel. Top. Quantum Electron.* 3 (1997) 1103-1111.

20. S.T. Fard, W. Hofmann, P.T. Fard, G. Bohm, M. Ortsiefer, E. Kwok, M.C. Amann, L. Chrostowski, Optical absorption glucose measurements using 2.3 μm vertical-cavity semiconductor lasers, *IEEE Photon. Technol. Lett.* 20 (2008) 930–932.
21. B. M. Walsh, N. P. Barnes, M. Petros, J. Yu, U. N. Singh, Spectroscopy and modeling of solid state lanthanide lasers: Application to trivalent Tm^{3+} and Ho^{3+} in YLiF_4 and LuLiF_4 , *J. Appl. Phys.* 95 (2004) 3255-3271.
22. R. L. Aggarwal, D. J. Ripin, J. R. Ochoa, T. Y. Fan, Measurement of thermo-optic properties of $\text{Y}_3\text{Al}_5\text{O}_{12}$, $\text{Lu}_3\text{Al}_5\text{O}_{12}$, YAlO_3 , LiYF_4 , LiLuF_4 , BaY_2F_8 , $\text{KGd}(\text{WO}_4)_2$, and $\text{KY}(\text{WO}_4)_2$ laser crystals in the 80–300 K temperature range, *J. Appl. Phys.* 98 (2005) 103514-1-14.
23. S. So, J. I. Mackenzie, D. P. Sheperd, W. A. Clarkson, J. G. Betterton, E. K. Gorton, A power-scaling strategy for longitudinally diode-pumped $\text{Tm}:\text{YLF}$ lasers, *Appl. Phys. B* 84 (2006) 389–393.
24. I. H. Malitson, A redetermination of some optical properties of calcium fluoride, *Appl. Opt.* 2 (1963) 1103-1107.
25. B. M. Walsh, N. P. Barnes, B. Di Bartolo, Branching ratios, cross sections, and radiative lifetimes of rare earth ions in solids: Application to Tm^{3+} and Ho^{3+} ions in LiYF_4 , *J. Appl. Phys.* 3 (1998) 2772-2787.
26. P. Loiko, J. M. Serres, X. Mateos, S. Tacchini, M. Tonelli, S. Veronesi, D. Parisi, A. Di Lieto, K. Yumashev, U. Griebner, V. Petrov, Comparative spectroscopic and thermo-optic study of $\text{Tm}:\text{LiLnF}_4$ ($\text{Ln} = \text{Y}, \text{Gd}, \text{and Lu}$) crystals for highly-efficient microchip lasers at $\sim 2 \mu\text{m}$, *Opt. Mater. Express* 7 (2017) 844-854.
27. P. Camy, J.L. Doualan, S. Renard, A. Braud, V. Ménard, R. Moncorgé, $\text{Tm}^{3+}:\text{CaF}_2$ for 1.9 μm laser operation, *Opt. Commun.* 236 (2004) 395-402.
28. M. Chen, P. Loiko, J. M. Serres, S. Veronesi, M. Tonelli, M. Aguiló, F. Díaz, J. E. Bae, T. G. Park, F. Rotermund, S. Dai, Z. Chen, U. Griebner, V. Petrov, X. Mateos, Fluorite-type $\text{Tm}^{3+}:\text{KY}_3\text{F}_{10}$: A promising crystal for watt-level lasers at $\sim 1.9 \mu\text{m}$, *J. Alloys Compd.* 813 (2020) 152176-1-8.
29. M. Schellhorn, High-power diode-pumped $\text{Tm}:\text{YLF}$ laser, *Appl. Phys. B* 91 (2008) 71–74.
30. F. Cornacchia, D. Parisi, M. Tonelli, “Spectroscopy and diode-pumped laser experiments of $\text{LiLuF}_4:\text{Tm}^{3+}$ crystals, *IEEE J. Quantum Electron.* 44 (2008) 1076-1082.
31. F. Cornacchia, D. Parisi, C. Bernardini, A. Toncelli, M. Tonelli, Efficient, diode-pumped $\text{Tm}^{3+}:\text{BaY}_2\text{F}_8$ vibronic laser, *Opt. Express* 12 (2004) 1982-1989.
32. A. Sottile, E. Damiano, M. Rabe, R. Bertram, D. Klimm, M. Tonelli, Widely tunable, efficient 2 μm laser in monocrystalline $\text{Tm}^{3+}:\text{SrF}_2$, *Opt. Express* 26 (2018) 5368-5380.
33. F. Cornacchia, A. Di Lieto, M. Tonelli, $\text{LiGdF}_4:\text{Tm}^{3+}$: spectroscopy and diode-pumped laser experiments, *Appl. Phys. B* 96 (2009) 363-368.
34. G. Galzerano, E. Sani, A. Toncelli, G. Della Valle, S. Taccheo, M. Tonelli, P. Laporta, Widely tunable continuous-wave diode-pumped 2- μm $\text{Tm}-\text{Ho}:\text{KYF}_4$ laser, *Opt. Lett.* 29 (2004) 715-717.
35. B. Cockayne, J. G. Plant, R. A. Clay, The Czochralski growth and laser characteristics of $\text{Li}(\text{Y}, \text{Er}, \text{Tm}, \text{Ho})\text{F}_4$ and $\text{Li}(\text{Lu}, \text{Er}, \text{Tm}, \text{Ho})\text{F}_4$ scheelite single crystals, *J. Cryst. Growth* 54 (1981) 407-413.
36. P. Loiko, R. Soulard, L. Guillemot, G. Brasse, J.-L. Doualan, A. Braud, A. Tyazhev, A. Hideur, B. Guichardaz, F. Druon, P. Camy, Efficient $\text{Tm}:\text{LiYF}_4$ lasers at $\sim 2.3 \mu\text{m}$: Effect of energy-transfer upconversion, *IEEE J. Quantum Electron.* 55 (2019) 1700212.

37. P.S.F. De Matos, N.U. Wetter, L. Gomes, I.M. Ranieri, S.L. Baldochi, A high power 2.3 μm Yb:Tm:YLF laser diode-pumped simultaneously at 685 and 960 nm, *J. Opt. A* 10 (2008) 104009-1-7.
38. L. Guillemot, P. Loiko, R. Soulard, A. Braud, J.-L. Doualan, A. Hideur, R. Moncorgé, P. Camy, Thulium laser at $\sim 2.3 \mu\text{m}$ based on upconversion pumping, *Opt. Lett.* 44 (2019) 4071-4074.
39. L. Guillemot, P. Loiko, R. Soulard, A. Braud, J.-L. Doualan, A. Hideur, P. Camy, Close look on cubic Tm:KY₃F₁₀ crystal for highly efficient lasing on the $^3\text{H}_4 \rightarrow ^3\text{H}_5$ transition, *Opt. Express* 28 (2020) 3451-3463.
40. A. Muti, M. Tonelli, V. Petrov, A. Sennaroglu, Continuous-wave mid-infrared laser operation of Tm³⁺:KY₃F₁₀ at 2.3 μm , *Opt. Lett.* 44 (2019) 3242–3245.
41. M. Diaf, A. Braud, C. Labbé J. L. Doualan, S. Girard, J. Margerie, R. Moncorgé, M. Thuaum, Synthesis and spectroscopic studies of Tm³⁺-doped KY₃F₁₀ single crystals, *Can. J. Phys.* 77 (2000) 693-697.
42. S. Renard, P. Camy, A. Braud, J.L. Doualan, R. Moncorgé, CaF₂ doped with Tm³⁺: A cluster model, *J. Alloys Compd* 451 (2008) 71-73.
43. X. Liu, K. Yang, S. Zhao, T. Li, C. Luan, X. Guo, B. Zhao, L. Zheng, L. Su, J. Xu, J. Bian, Growth and lasing performance of a Tm,Y:CaF₂ crystal, *Opt. Lett.* 42 (2017) 2567-2570.
44. L.H. Guilbert, J.Y. Gesland, A. Bulou, R. Retoux, Structure and Raman spectroscopy of Czochralski-grown barium yttrium and barium ytterbium fluorides crystals, *MRS Bull.* 28 (1993) 923-930.
45. H. Scheife, G. Huber, E. Heumann, S. Bär, E. Osiaç, Advances in up-conversion lasers based on Er³⁺ and Pr³⁺, *Opt. Mater.* 26 (2004) 365-374.
46. N.P. Barnes, D.J. Gettemy, Temperature variation of the refractive indices of yttrium lithium fluoride, *J. Opt. Soc. Am.* 70 (1980) 1244-1247.
47. J.J. Owen, A.K. Cheetham, R.A. McFarlane, Orientation-dependent fluorescence studies and spectroscopic analysis of doped barium yttrium fluoride upconversion laser crystals (BaY_{2-x-y}Yb_xTm_yF₈), *J. Opt. Soc. Am. B* 15 (1998) 684-693.
48. A.A. Kaminskii, O. Lux, J. Hanuza, H. Rhee, H.J. Eichler, J. Zhang, D. Tang, D. Shen, H. Yu, J. Wang, H. Yoneda, Monoclinic β -BaY₂F₈—a novel crystal simultaneously active for SRS and Ln³⁺-ion lasing, *Laser Phys.* 25 (2014) 015801.
49. B. Aull, H. Janssen, “Vibronic interactions in Nd:YAG resulting in nonreciprocity of absorption and stimulated emission cross sections, *IEEE J. Quantum Electron.* 18 (1982) 925-930.
50. A. Braud, Caractéristiques spectroscopiques et émission laser de l’ion Tm³⁺ à 1.5 μm dans les fluorures, PhD thesis, University of Caen, France, Oct. 1999.
51. R. Soulard, J.L. Doualan, A. Braud, M. Sahli, A. Benayad, G. Brasse, A. Hideur, A. Tyazhev, R. Moncorgé, P. Camy, 1.87 μm laser operation by 980 nm pumping in Yb,Tm:CaF₂, *Opt. Mat.* 72 (2017) 578-582.
52. J. Xiong, H.Y. Peng, C.C. Zhao, Y. Hang, L.H. Zhang, M.Z. He, X.M. He, G.Z. Chen, Crystal growth, spectroscopic characterization, and laser performance of Tm:LiLuF₄ crystal, *Laser Phys. Lett.* 6 (2009) 868–871.
53. F. Cornacchia, D. Parisi, M. Tonelli, Spectroscopy and diode-pumped laser experiments of LiLuF₄:Tm³⁺ crystals, *IEEE J. Quantum Electron.* 44 (2008) 1076-1082.
54. B.R. Judd, Optical absorption intensities of rare-earth ions, *Phys. Rev.* 127 (1962) 750–761.

55. G.S. Ofelt, Intensities of crystal spectra of rare-earth ions, *J. Chem. Phys.* 37 (1962) 511–520.
56. A.A. Kornienko, A.A. Kaminskii, E.B. Dunina, Dependence of the line strength of f–f transitions on the manifold energy. II. Analysis of Pr³⁺ in KPrP₄O₁₂, *Phys. Status Solidi B* 157 (1990) 267-273.
57. P. Loiko, A. Volokitina, X. Mateos, E. Dunina, A. Kornienko, E. Vilejshikova, M. Aguilo, F. Diaz, Spectroscopy of Tb³⁺ ions in monoclinic KLu(WO₄)₂ crystal: application of an intermediate configuration interaction theory, *Opt. Mater.* 78 (2018) 495-501.
58. P.A. Loiko, A.S. Yasukevich, A.E. Gulevich, M.P. Demesh, M.B. Kosmyna, B.P. Nazarenko, V.M. Puzikov, A.N. Shekhovtsov, A.A. Kornienko, E.B. Dunina, N.V. Kuleshov, K.V. Yumashev, Growth, spectroscopic and thermal properties of Nd-doped disordered Ca₉La(VO₄)₇ and Ca₁₀(Li/K)(VO₄)₇ laser crystals, *J. Lumin.* 137 (2013) 252-258.
59. L. Zhang, H. Lin, G. Zhang, X. Mateos, J. M. Serres, M. Aguiló, F. Díaz, U. Griebner, V. Petrov, Y. Wang, P. Loiko, E. Vilejshikova, K. Yumashev, Z. Lin, W. Chen, Crystal growth, optical spectroscopy and laser action of Tm³⁺-doped monoclinic magnesium tungstate, *Opt. Express* 25 (2017) 3682-3693.
60. P.S. Peijzel, P. Vergeer, A. Meijerink, M.F. Reid, L.A. Boatner, G.W. Burdick, 4ⁿ-15d → 4ⁿ emission of Ce³⁺, Pr³⁺, Nd³⁺, Er³⁺, and Tm³⁺ in LiYF₄ and YPO₄, *Phys. Rev. B* 71 (2005) 045116-1-9.
61. P. Dorenbos, The 5d level positions of the trivalent lanthanides in inorganic compounds, *J. Lumin.* 91 (2000) 155-176.
62. S. Luo, R. Moncorgé, J.L. Doualan, H. Xu, Z. Cai, C. Labbé, B. Xu, A. Braud, P. Camy, Simulation of dual-wavelength pumped 3.5 μm CW laser operation of Er:CaF₂ and Er:KY₃F₁₀ in waveguide configuration, *J. Opt. Soc. Am. B* 36 (2019) 275-284.
63. D.S. Pytalev, S.A. Klimin, M.N. Popova, Optical high-resolution spectroscopic study of Tm³⁺ crystal-field levels in LiLuF₄, *J. Rare Earths* 27 (2009) 624-626.

List of figure captions

Figure 1. Energy level scheme for Tm^{3+} ions (Stark splittings for $\text{Tm}:\text{LiYF}_4$ can be found in [2]) showing processes relevant for laser operation in the near- and mid-IR: green and red arrows - pump and laser transitions, respectively; R and NR - radiative and non-radiative relaxation, respectively; CR - cross-relaxation, ETU – energy-transfer upconversion, EM – energy-migration.

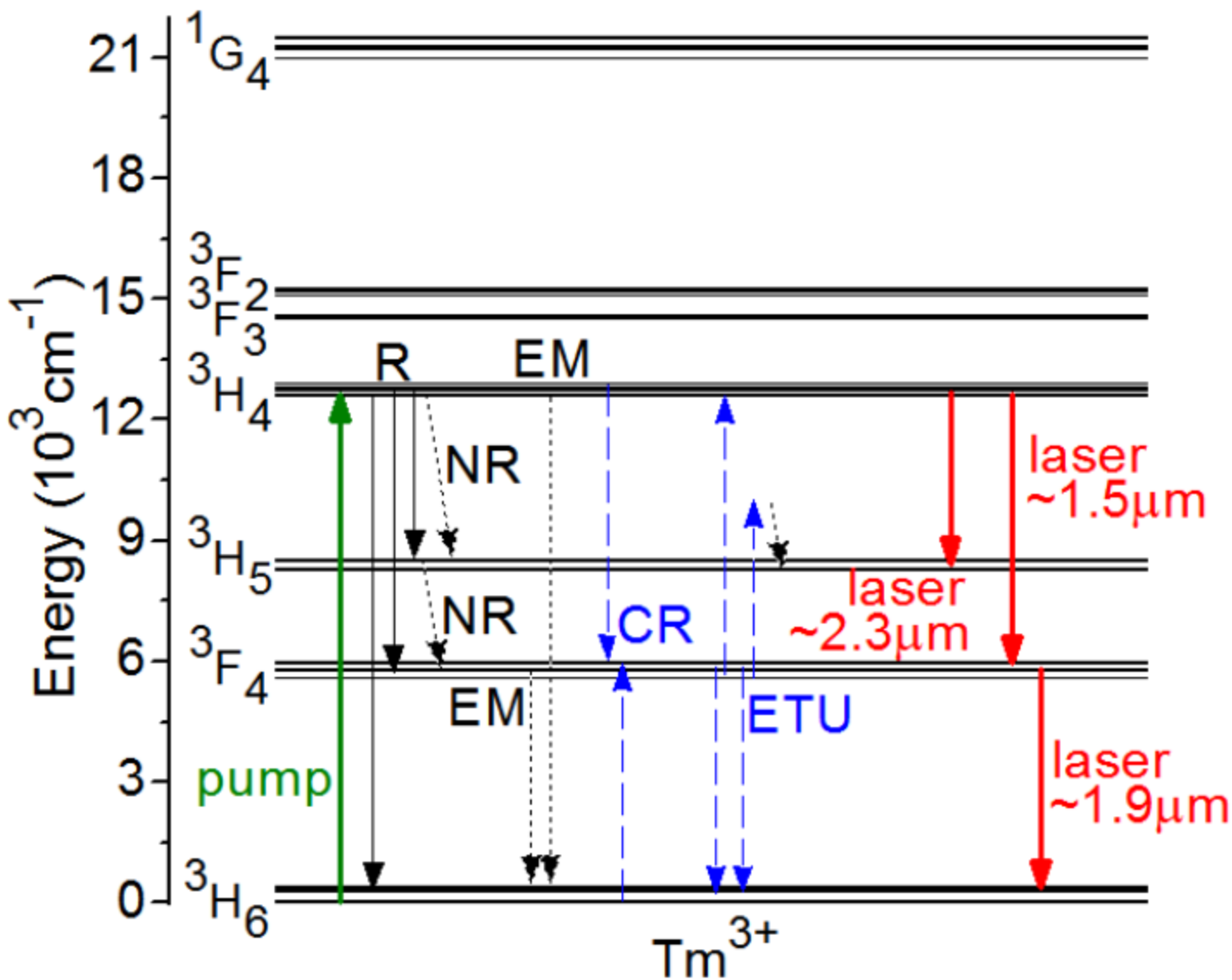
Figure 2. Optical orientation of LiLnF_4 ($\text{Ln} = \text{Y}, \text{Lu}$) and BaY_2F_8 crystals: (*a*, *b*, *c*) – crystallographic axes, O.A. – optical axis, (X, Y, Z) – optical indicatrix axes, *n* – refractive indices.

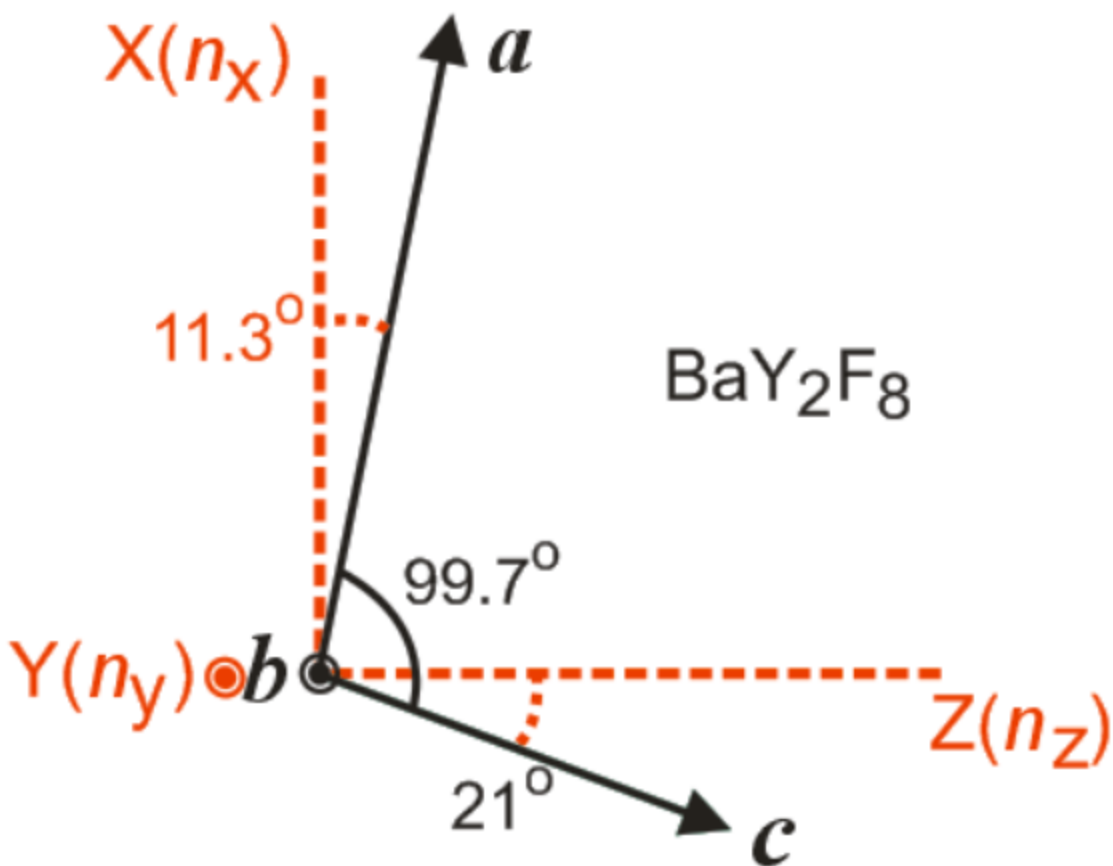
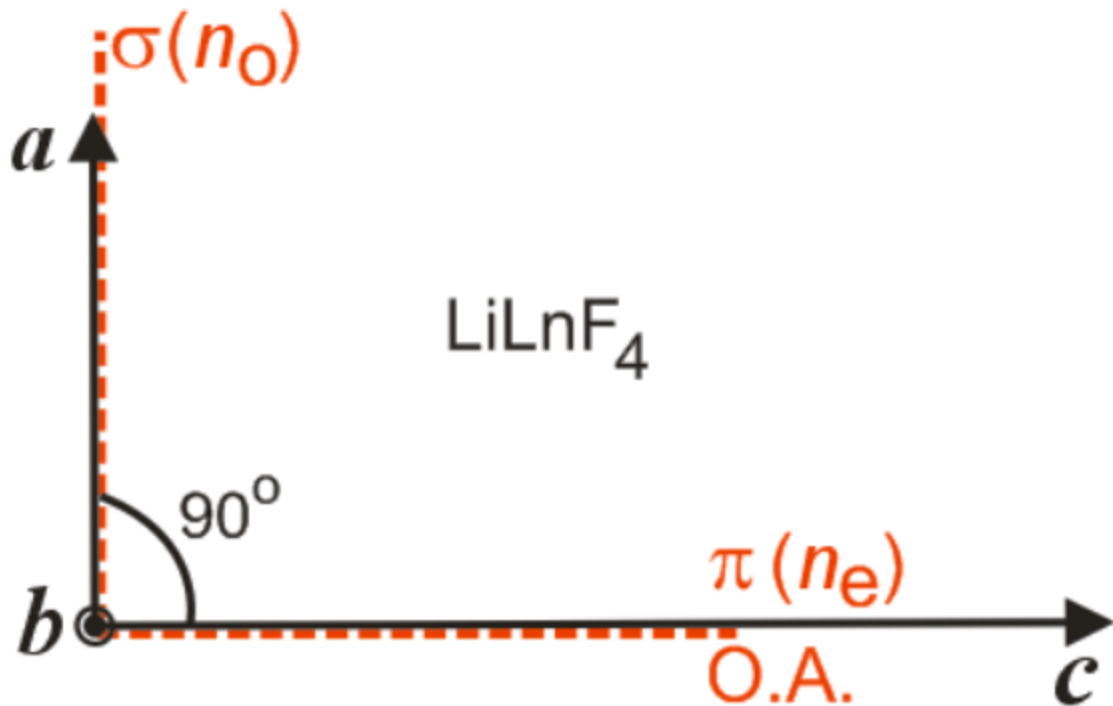
Figure 3. Absorption cross-section spectra, σ_{abs} , for the ${}^3\text{H}_6 \rightarrow {}^3\text{H}_4$ pump transition of Tm^{3+} ions in (a) cubic crystals KY_3F_{10} and CaF_2 , (b) tetragonal crystals LiYF_4 and LiLuF_4 and (c) monoclinic crystal BaY_2F_8 .

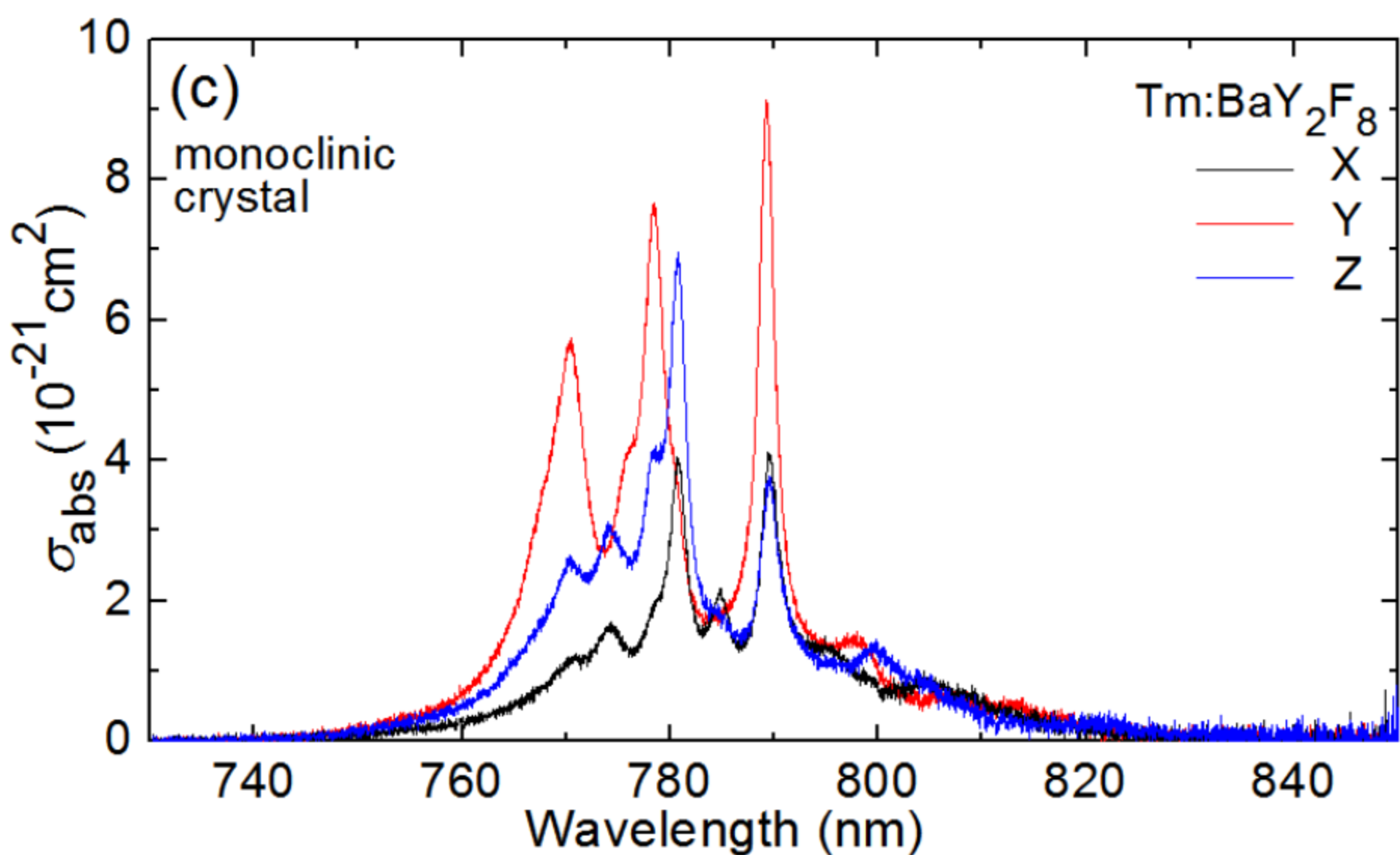
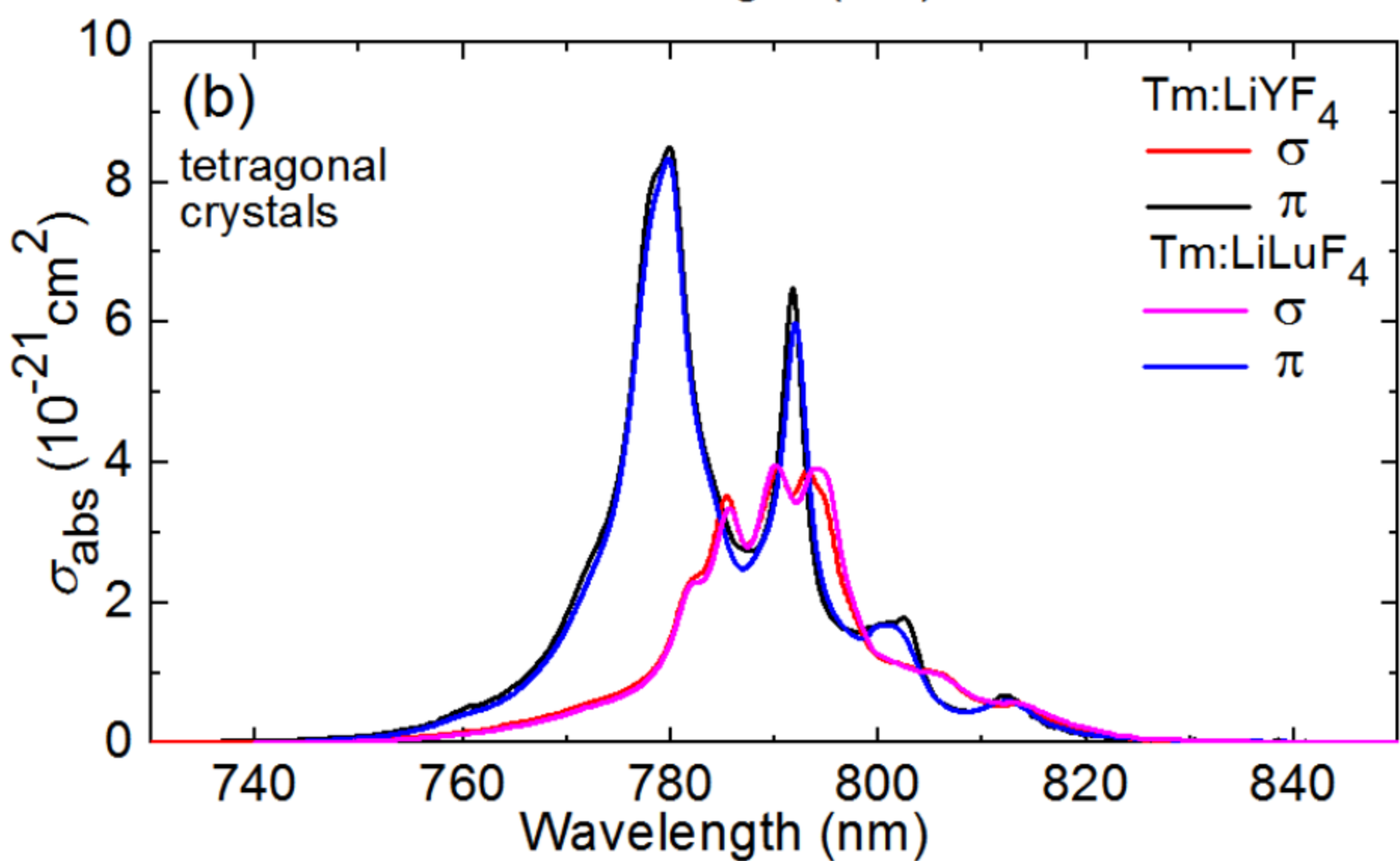
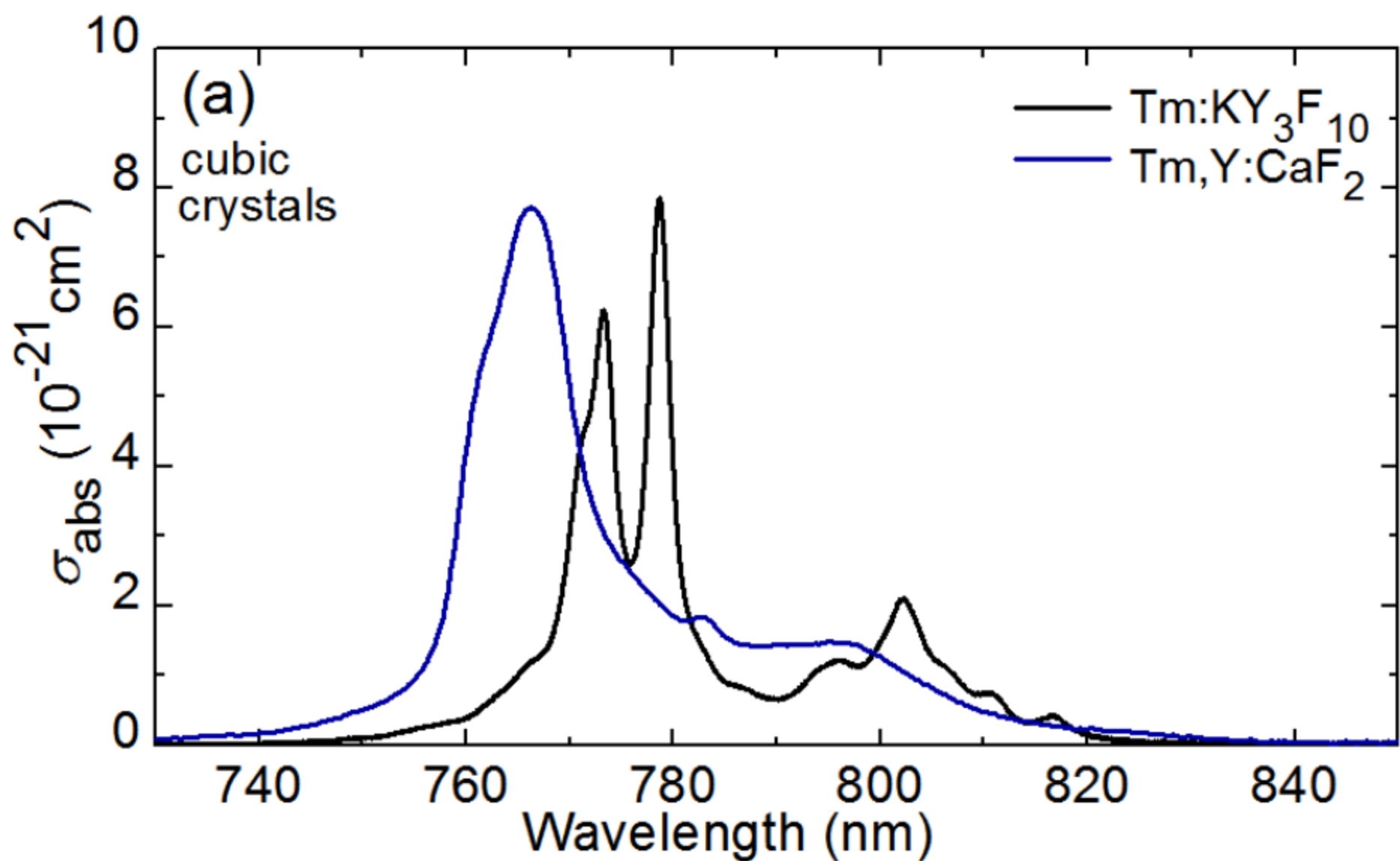
Figure 4. Stimulated-emission (SE) cross-section spectra, σ_{SE} , for the ${}^3\text{H}_4 \rightarrow {}^3\text{F}_4$ transition of Tm^{3+} ions around $1.45 \mu\text{m}$ in (a) cubic crystals KY_3F_{10} and CaF_2 , (b) tetragonal crystals LiYF_4 and LiLuF_4 and (c) monoclinic crystal BaY_2F_8 .

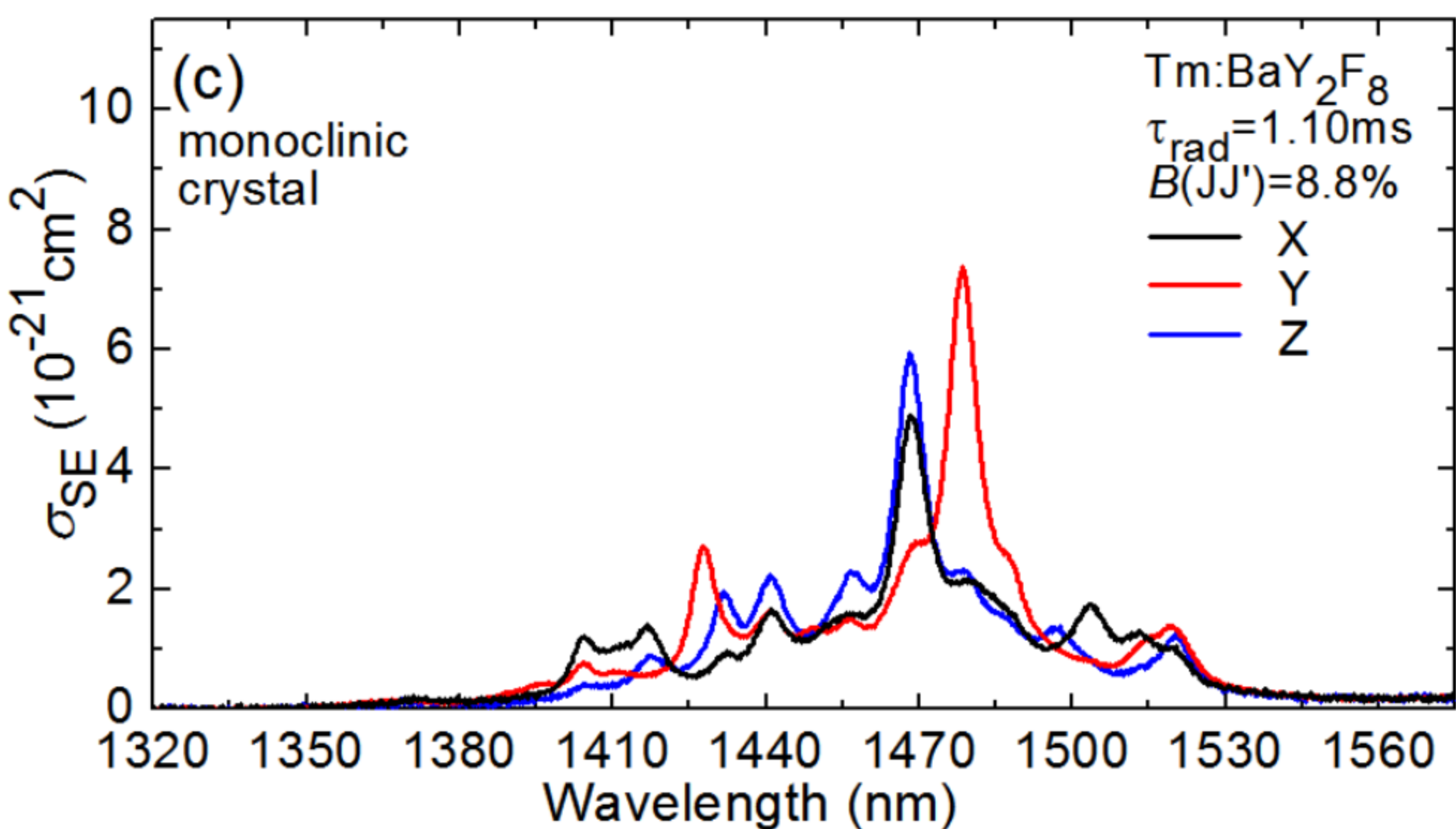
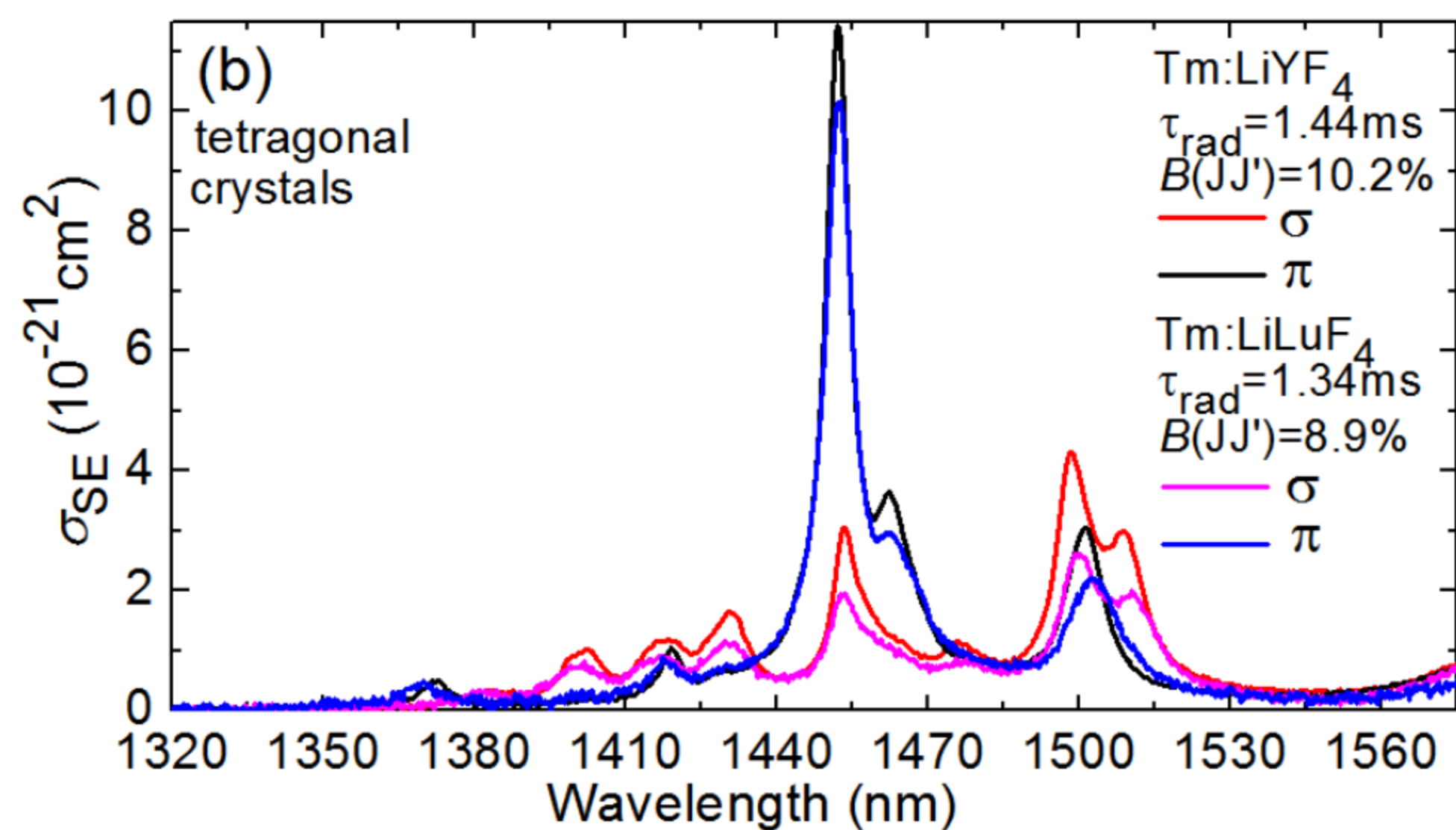
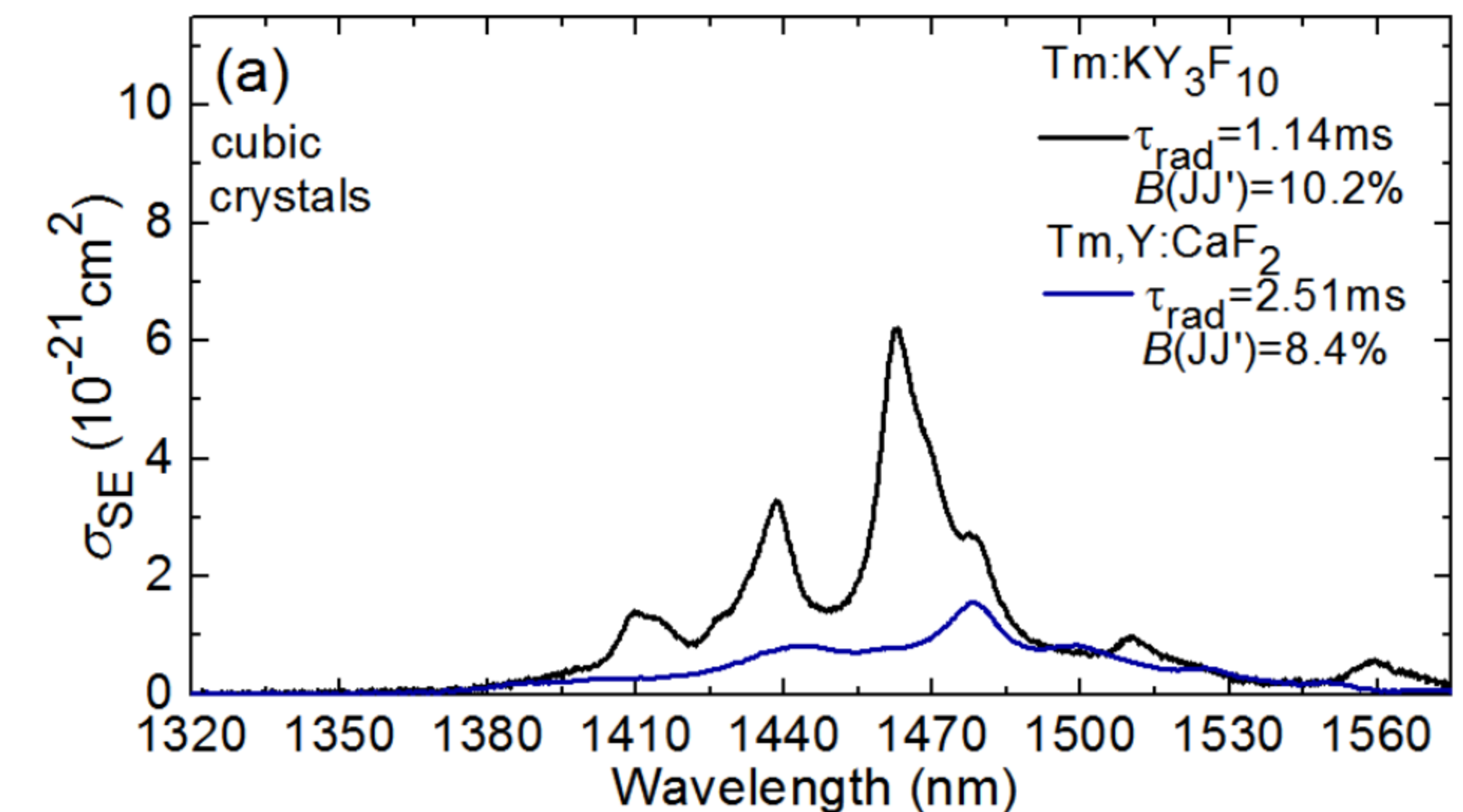
Figure 5. Stimulated-emission (SE) cross-section spectra, σ_{SE} , for the ${}^3\text{H}_4 \rightarrow {}^3\text{H}_5$ transition of Tm^{3+} ions around $2.3 \mu\text{m}$ in (a) cubic crystals KY_3F_{10} and CaF_2 , (b) tetragonal crystals LiYF_4 and LiLuF_4 and (c) monoclinic crystal BaY_2F_8 .

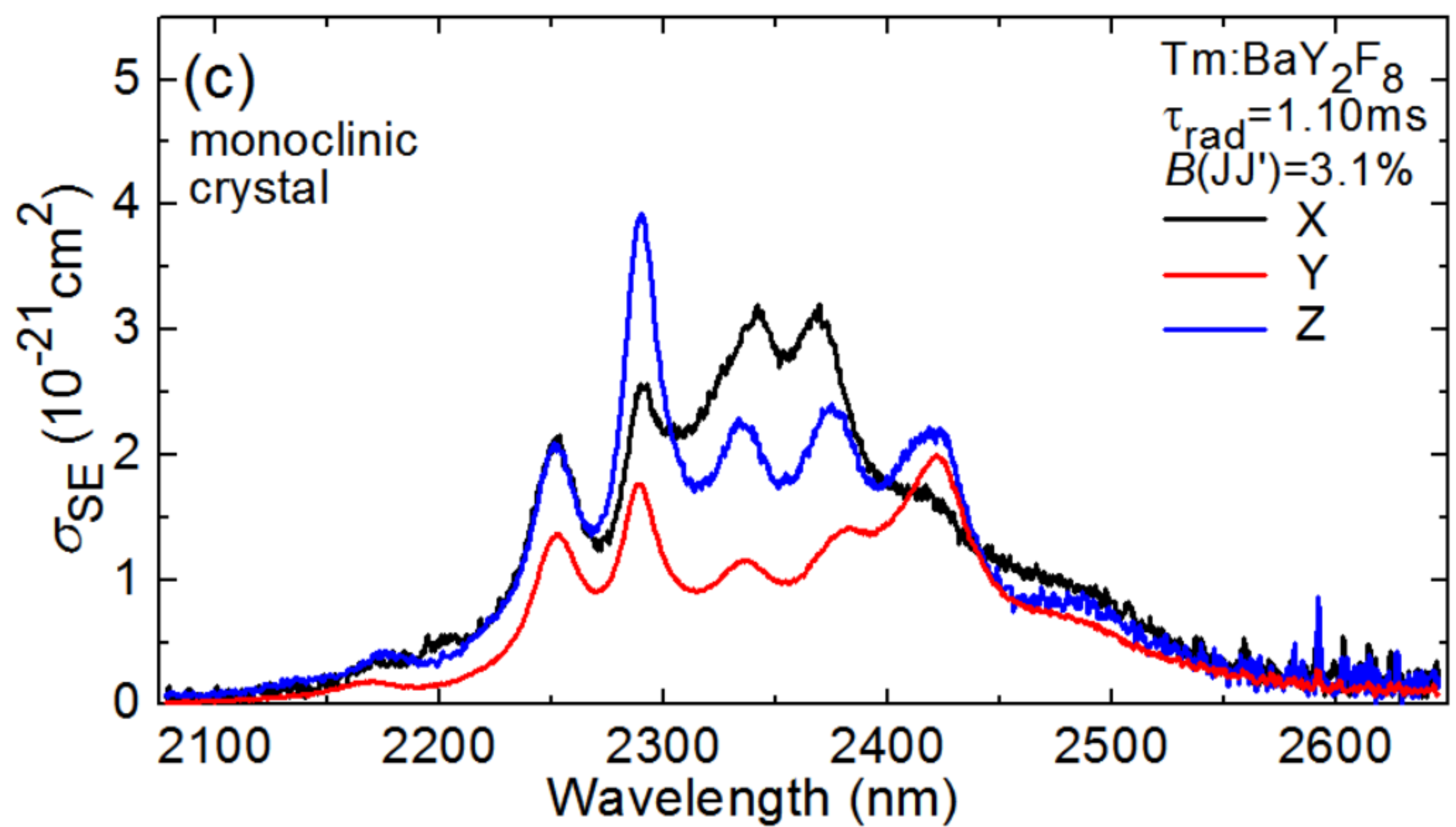
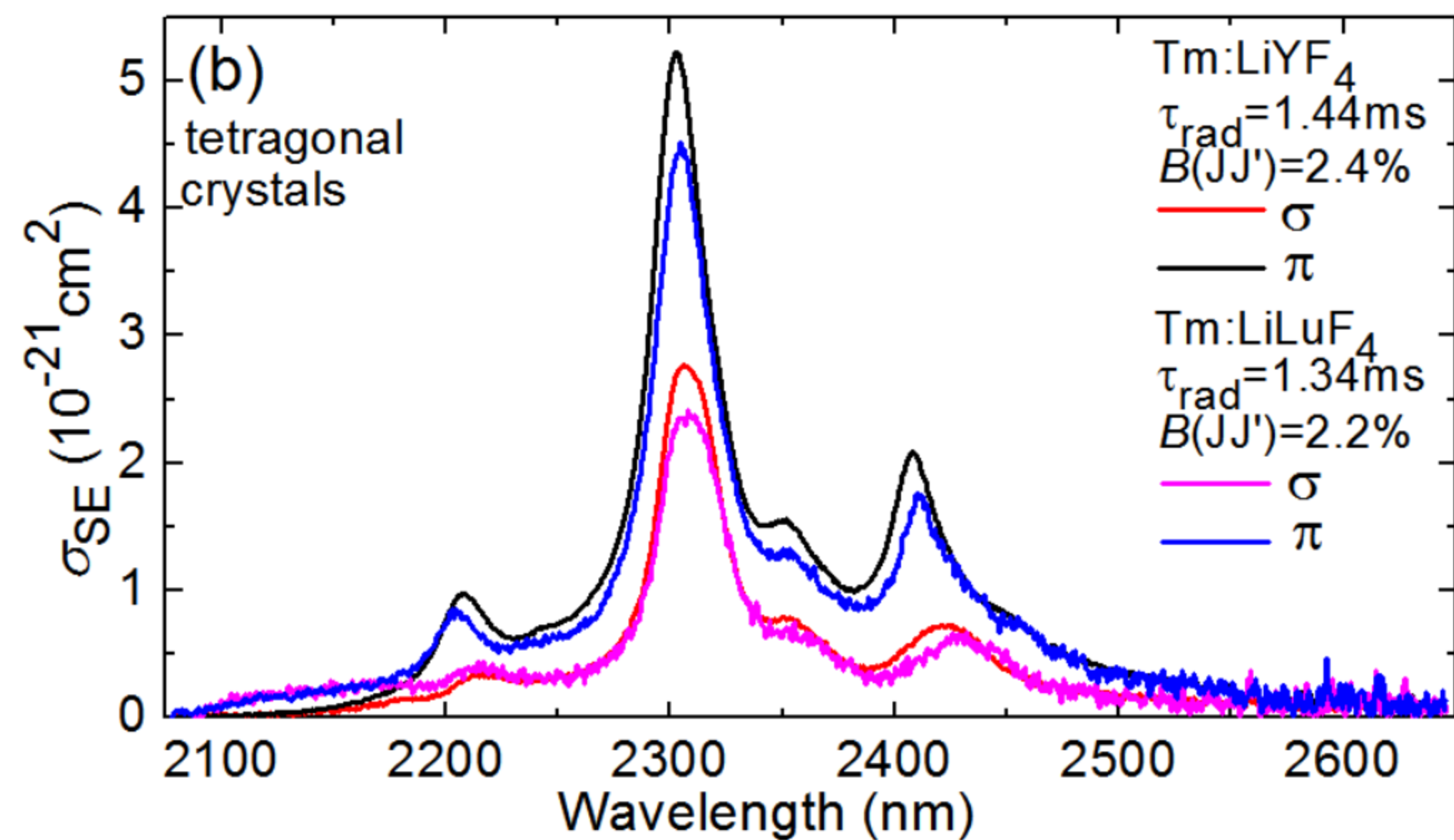
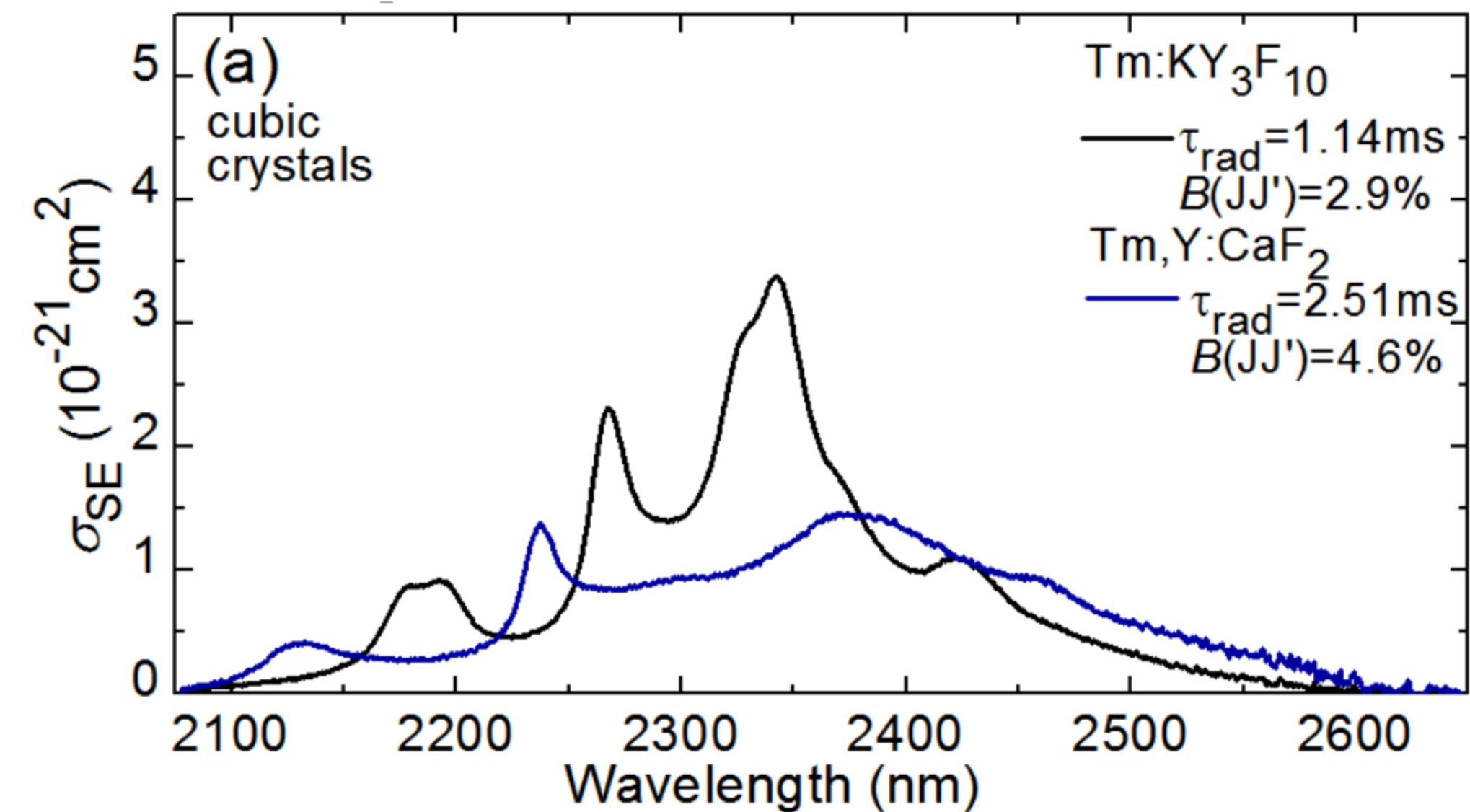
Figure 6. Overview absorption cross-section spectra, σ_{abs} , of (a) $\text{Tm}:\text{LiLuF}_4$ crystal for light polarizations π and σ ; and (b) $\text{Tm}:\text{BaY}_2\text{F}_8$ crystal for light polarizations $E \parallel X, Y, Z$.











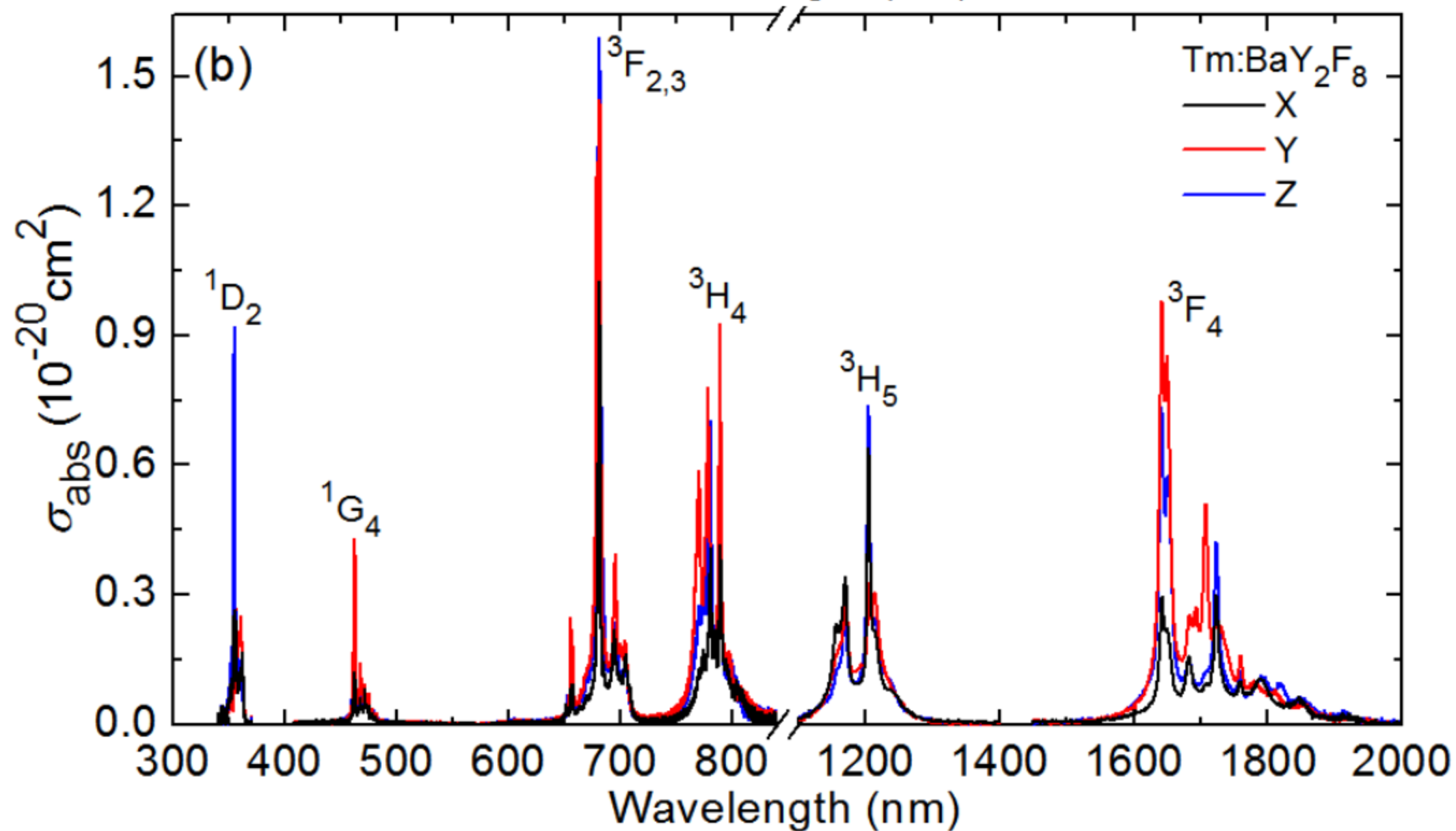
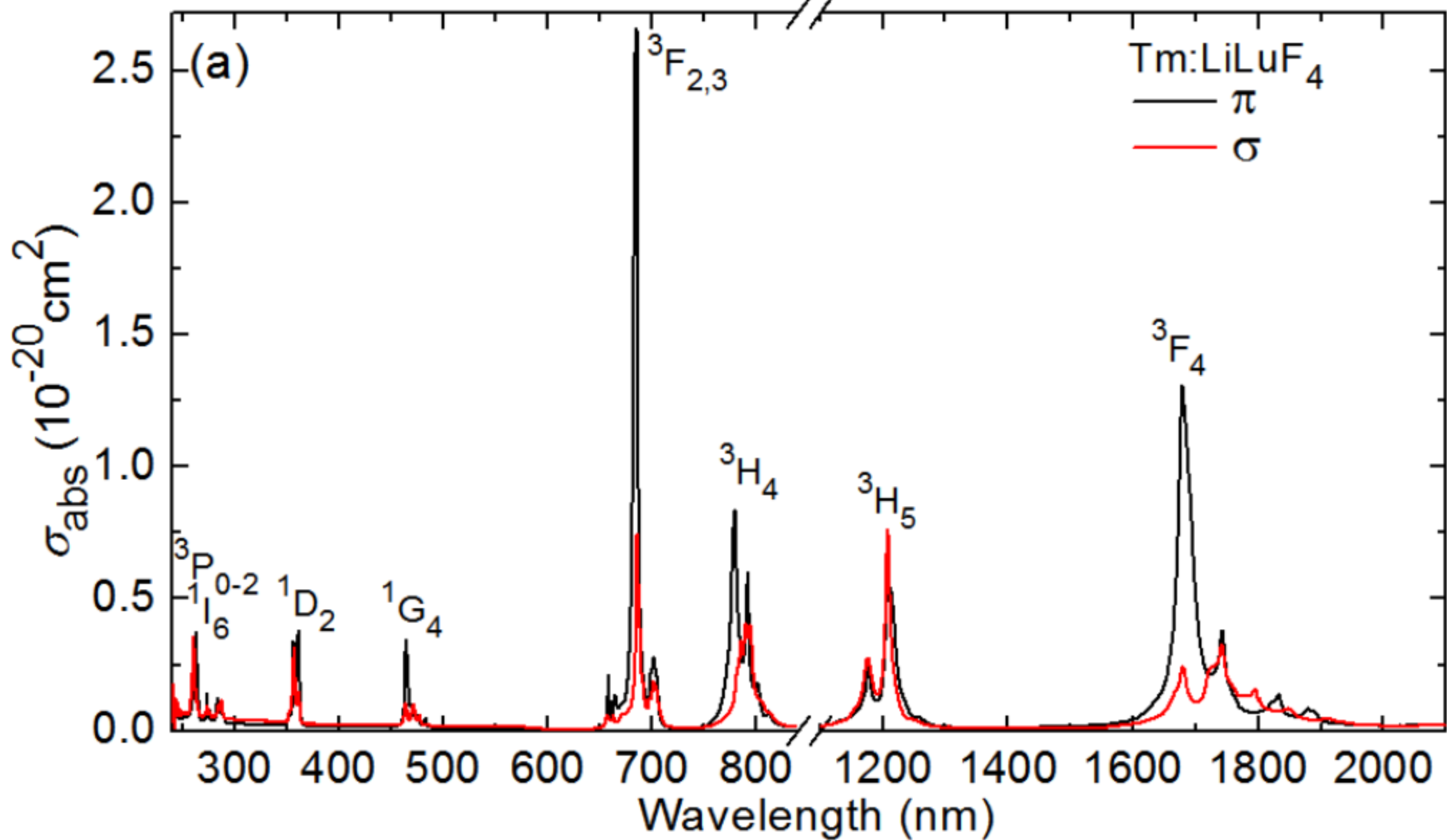


Table 1. Structural properties of the studied fluoride laser crystals.

Crystal	Growth *	T_{melting} , °C	Crystal class (sp. gr.)	Optical behavior	Tm^{3+} site	N_{Tm} ,** 10^{20} cm^{-3}	$h\nu_{\text{ph}}$, cm^{-1}
CaF_2	Br	1360	cubic ($\text{O}_h^5 - Fm\bar{3}m$)	isotropic	cluster	2.45	495
KY_3F_{10}	Cz	1030	cubic ($\text{O}_h^5 - Fm\bar{3}m$)	isotropic	$\text{C}_{4v}(\text{Y}^{3+})$	1.56	495
LiYF_4	Cz	842	tetragonal ($\text{C}_{4h}^6 - I4_1/a$)	uniaxial	$\text{S}_4(\text{Y}^{3+})$	1.38	446
LiLuF_4	Cz	825	tetragonal ($\text{C}_{4h}^6 - I4_1/a$)	uniaxial	$\text{S}_4(\text{Lu}^{3+})$	1.43	435
BaY_2F_8	Cz	960	monoclinic ($\text{C}_{2h}^3 - C2/m$)	biaxial	$\text{C}_2(\text{Y}^{3+})$	1.30	421

*Cz – Czochralski method, Br – Bridgman method.

**For 1 at.% doping level.

Table 2. Absorption properties of Tm^{3+} ions in fluoride crystals corresponding to the ${}^3\text{H}_6 \rightarrow {}^3\text{H}_4$ transition at around $0.8 \mu\text{m}$.

Crystal	$\sigma_{\text{abs}}, 10^{-20} \text{ cm}^2$	$\lambda_{\text{abs}}, \text{ nm}$	$\Delta\lambda_{\text{abs}}, \text{ nm}$
CaF_2	0.77	766.1	11.9
KY_3F_{10}	0.79	778.6	2.8
LiYF_4	0.85 (π),	779.9 (π),	7.6 (π),
	0.39 (σ)	790.3 (σ)	16.5 (σ)
LiLuF_4	0.81 (π),	781.8 (π),	7.1 (π),
	0.40 (σ)	790.1 (σ)	16.6 (σ)
BaY_2F_8	0.40 (X),	780.7 (X),	3.4 (X),
	0.90 (Y),	789.3 (Y),	2.1 (Y),
	0.69 (Z)	780.7 (Z)	4.3 (Z)

* σ_{abs} – absorption cross-section, λ_{abs} - peak absorption wavelength, $\Delta\lambda_{\text{abs}}$ - absorption bandwidth. The light polarization is indicated in brackets.

Table 3. Radiative lifetime of the ${}^3\text{H}_4$ state τ_{rad} and the luminescence branching ratios $B(\text{JJ}')$ used for calculating the SE cross-sections for the ${}^3\text{H}_4 \rightarrow {}^3\text{H}_5$ and ${}^3\text{H}_4 \rightarrow {}^3\text{F}_4$ transitions of Tm^{3+} ions in fluoride crystals.

Crystal	$\tau_{\text{rad}}({}^3\text{H}_4)$, ms	$B(\text{JJ}')$, %		$*\Omega_k \times 10^{20}$, cm^2			Ref.
		${}^3\text{H}_4 \rightarrow {}^3\text{H}_5$	${}^3\text{H}_4 \rightarrow {}^3\text{F}_4$	Ω_2	Ω_4	Ω_6	
CaF_2	2.51	4.6	8.4	0.891	1.251	0.959	[51]
KY_3F_{10}	1.14	2.9	10.2	1.907	1.531	1.465	[41]
LiYF_4	1.44	2.4	10.2	1.96	1.17	1.38	[50]
LiLuF_4	1.34	2.2	8.9	**			This work
BaY_2F_8	1.10	3.1	8.8	**			This work

*The J-O parameters Ω_k ($k = 2, 4, 6$) corresponding to the τ_{rad} and $B(\text{JJ}')$ values are given.

**Spectroscopic parameters calculated within the ICI approximation, cf. Table 7 for the full list of intensity parameters.

Table 4. Emission properties of Tm^{3+} ions in fluoride crystals corresponding to the ${}^3\text{H}_4 \rightarrow {}^3\text{H}_5$ and ${}^3\text{H}_4 \rightarrow {}^3\text{F}_4$ transitions in emission at $\sim 1.5 \mu\text{m}$ and $\sim 2.3 \mu\text{m}$, respectively.

Crystal	${}^3\text{H}_4 \rightarrow {}^3\text{H}_5$			${}^3\text{H}_4 \rightarrow {}^3\text{F}_4$	
	$\sigma_{\text{SE}}, 10^{-20} \text{ cm}^2$	$\lambda_{\text{em}}, \text{ nm}$	$\Delta\lambda_{\text{em}}, \text{ nm}$	$\sigma_{\text{SE}}, 10^{-20} \text{ cm}^2$	$\lambda_{\text{em}}, \text{ nm}$
CaF_2	0.15	2372	252	0.16	1478
KY_3F_{10}	0.34	2342	62	0.62	1462
LiYF_4	0.52 (π),	2303 (π),	34 (π),	1.14 (π),	1452 (π),
	0.28 (σ)	2306 (σ)	34 (σ)	0.31 (σ)	1498 (σ)
LiLuF_4	0.44 (π),	2304 (π),	35 (π),	1.01 (π),	1452 (π),
	0.23 (σ)	2307 (σ)	36 (σ)	0.26 (σ)	1500 (σ)
BaY_2F_8	0.32 (X),	2341 (X),	144 (X),	0.49 (X),	1468 (X),
	0.20 (Y)	2421 (Y)	86 (Y),	0.73 (Y),	1478 (Y),
	0.39 (Z)	2289 (Z)	29(Z)	0.58 (Z)	1468 (Z)

* σ_{SE} - stimulated-emission cross-section, λ_{em} - peak emission wavelength, $\Delta\lambda_{\text{em}}$ - emission bandwidth. The light polarization is indicated in brackets.

Table 5. Experimental and calculated absorption oscillator strengths* for Tm³⁺ ions in the LiLuF₄ crystal.

³ H ₆ → ² S+ ¹ L _J	<i>E_J</i> , cm ⁻¹	$\langle f_{\text{exp}} \rangle$ ×10 ⁶	$\langle f_{\text{calc}}^2 \rangle \times 10^6$		
			J-O	mJ-O	ICI
³ F ₄	5700	1.436	1.588 ^{ED}	1.565 ^{ED}	1.375 ^{ED}
³ H ₅	8335	1.571	1.150 ^{ED+} 0.406 ^{MD}	1.134 ^{ED+} 0.406 ^{MD}	1.212 ^{ED+} 0.406 ^{MD}
³ H ₄	12594	1.970	1.842 ^{ED}	1.865 ^{ED}	2.033 ^{ED}
³ F _{2,3}	14504	2.619	2.563 ^{ED}	2.539 ^{ED}	2.568 ^{ED}
¹ G ₄	21160	0.593	0.558 ^{ED}	0.568 ^{ED}	0.593 ^{ED}
¹ D ₂	27944	1.596	1.839 ^{ED}	1.832 ^{ED}	1.699 ^{ED}
¹ I ₆ + ³ P ₀	35084	0.769	0.699 ^{ED+} 0.021 ^{MD}	0.729 ^{ED+} 0.021 ^{MD}	0.617 ^{ED+} 0.021 ^{MD}
³ P ₁	36368	0.214	0.522 ^{ED}	0.551 ^{ED}	0.288 ^{ED}
³ P ₂	38009	2.125	1.916 ^{ED}	1.941 ^{ED}	2.084 ^{ED}
<i>r.m.s. dev.</i>			0.202	0.219	0.126

**E_J* – barycenter energy of the absorption band, $\langle f_{\text{exp}} \rangle$ and $\langle f_{\text{calc}}^2 \rangle$ – experimental and calculated absorption oscillator strengths, respectively (ED + MD), the brackets $\langle .. \rangle$ indicate polarization-averaging, $1/3(2\sigma+\pi)$. ED and MD stand for electric-dipole and magnetic-dipole contributions, respectively.

Table 6. Experimental and calculated absorption oscillator strengths* for Tm^{3+} ions in the BaY_2F_8 crystal.

${}^3\text{H}_6 \rightarrow$ ${}^{2\text{S}+1}\text{L}_\text{J}$	$E_\text{J},$ cm^{-1}	$\langle f_{\text{exp}} \rangle$ $\times 10^6$	$\langle f_{\text{calc}}^2 \rangle \times 10^6$		
			J-O	mJ-O	ICI
${}^3\text{F}_4$	5812	1.596	2.007 ^{ED}	1.670 ^{ED}	1.602 ^{ED}
${}^3\text{H}_5$	8381	1.832	1.372 ^{ED+} 0.417 ^{MD}	1.210 ^{ED+} 0.417 ^{MD}	1.366 ^{ED+} 0.417 ^{MD}
${}^3\text{H}_4$	12738	2.289	1.905 ^{ED}	2.236 ^{ED}	2.295 ^{ED}
${}^3\text{F}_{2,3}$	14733	2.974	3.177 ^{ED}	3.058 ^{ED}	2.987 ^{ED}
${}^1\text{G}_4$	21164	0.751	0.715 ^{ED}	0.864 ^{ED}	0.765 ^{ED}
${}^1\text{D}_2$	28120	3.234	3.017 ^{ED}	3.199 ^{ED}	3.232 ^{ED}
<i>r.m.s. dev.</i>			<i>0.319</i>	<i>0.154</i>	<i>0.054</i>

* E_J – barycenter energy of absorption band, $\langle f_{\text{exp}} \rangle$ and $\langle f_{\text{calc}}^2 \rangle$ – experimental and calculated absorption oscillator strengths, respectively (ED + MD), the brackets $\langle \dots \rangle$ indicate polarization-averaging, $1/3(X+Y+Z)$. ED and MD stand for electric-dipole and magnetic-dipole contributions, respectively.

Table 7. Intensity parameters for Tm^{3+} ions in the LiLuF_4 and BaY_2F_8 crystals obtained within the standard J-O theory, the modified J-O theory (mJ-O) and the intermediate configuration interaction (ICI) approximation.

Crystal	Model	$\Omega_k \times 10^{20}, \text{cm}^2$			$\alpha \times 10^4,$	$R_k \times 10^4, \text{cm}$		
		Ω_2	Ω_4	Ω_6	cm	R_2	R_4	R_6
Tm:LiLuF ₄	J-O	2.224	1.602	1.042	-	-	-	-
	mJ-O	2.370	1.556	1.062	0.011	-	-	-
	ICI	2.920	1.331	1.006	-	0.072	0.099	-0.134
Tm:BaY ₂ F ₈	J-O	1.709	2.736	1.035	-	-	-	-
	mJ-O	3.396	2.358	1.345	0.110	-	-	-
	ICI	2.746	2.285	1.028	-	-0.012	0.211	-0.160

Table 8. Probabilities of radiative spontaneous transitions* for Tm³⁺ ions in LiLuF₄ (as calculated within the ICI approximation).

Excited state	Terminal state	$\langle\lambda\rangle$, nm	$A_{\Sigma}^{\text{calc}}(JJ')$, s ⁻¹	$B(JJ')$, %	A_{tot} , s ⁻¹	τ_{rad} , ms
³ F ₄	³ H ₆	1754	91.0 ^{ED}	100	91.0	10.99
³ H ₅	³ F ₄	3795	4.6 ^{ED} +0.1 ^{MD}	2.4	192.9	5.18
	³ H ₆	1200	141.0 ^{ED} +47.2 ^{MD}	97.6		
³ H ₄	³ H ₅	2348	11.6 ^{ED} +4.5 ^{MD}	2.2	745.0	1.34
	³ F ₄	1451	54.4 ^{ED} +11.9 ^{MD}	8.9		
	³ H ₆	794	662.6 ^{ED}	88.9		
³ F ₂ + ³ F ₃	³ H ₄	5236	4.7 ^{ED} +0.1 ^{MD}	0.2	2087.0	0.48
	³ H ₅	1621	231.7 ^{ED}	11.1		
	³ F ₄	1136	320.9 ^{ED} +31.0 ^{MD}	16.9		
	³ H ₆	689	1498.4 ^{ED}	71.8		
¹ G ₄	³ F ₂ + ³ F ₃	1502	36.1 ^{ED} +2.1 ^{MD}	3.2	1192.8	0.84
	³ H ₄	1167	111.8 ^{ED} +17.8 ^{MD}	10.9		
	³ H ₅	780	314.0 ^{ED} +70.5 ^{MD}	32.2		
	³ F ₄	647	83.1 ^{ED} +5.4 ^{MD}	7.4		
	³ H ₆	472	552.0 ^{ED}	46.3		
¹ D ₂	¹ G ₄	1474	140.9 ^{ED}	0.8	17396.4	0.058
	³ F ₂ + ³ F ₃	744	1576.7 ^{ED} +91.4 ^{MD}	9.5		
	³ H ₄	651	896.8 ^{ED}	5.2		
	³ H ₅	510	39.5 ^{ED}	0.2		
	³ F ₄	450	9628.4 ^{ED}	55.4		
	³ H ₆	358	5022.7 ^{ED}	28.9		

* $\langle\lambda\rangle$ - calculated mean emission wavelength, A_{Σ}^{calc} - probability of radiative spontaneous transitions (ED + MD), $B(JJ')$ - luminescence branching ratio, A_{tot} and τ_{rad} - total probability of radiative spontaneous transitions (ED+MD) and radiative lifetime of the excited state, respectively. ED and MD stand for electric-dipole and magnetic-dipole transitions, respectively.

Table 9. Probabilities of radiative spontaneous transitions* for Tm³⁺ ions in BaY₂F₈ (as calculated within the ICI approximation).

Excited state	Terminal state	$\langle\lambda\rangle$, nm	$A_{\Sigma}^{\text{calc}}(JJ)$, s ⁻¹	$B(JJ)$, %	A_{tot} , s ⁻¹	τ_{rad} , ms
³ F ₄	³ H ₆	1721	115.2 ^{ED}	100	115.2	8.68
³ H ₅	³ F ₄	3893	5.1 ^{ED} +0.1 ^{MD}	2.3	224.0	4.47
	³ H ₆	1193	167.6 ^{ED} +51.2 ^{MD}	97.7		
³ H ₄	³ H ₅	2295	22.7 ^{ED} +5.1 ^{MD}	3.1	906.4	1.10
	³ F ₄	1444	67.1 ^{ED} +12.9 ^{MD}	8.8		
	³ H ₆	785	798.6 ^{ED}	88.1		
³ F ₂ + ³ F ₃	³ H ₄	5012	5.9 ^{ED} +0.0 ^{MD}	0.2	2501.7	0.40
	³ H ₅	1574	299.5 ^{ED}	12.0		
	³ F ₄	1121	351.3 ^{ED} +31.4 ^{MD}	15.3		
	³ H ₆	679	1813.6 ^{ED}	72.5		
¹ G ₄	³ F ₂ + ³ F ₃	1555	56.0 ^{ED} +2.2 ^{MD}	4.1	1406.1	0.71
	³ H ₄	1187	93.1 ^{ED} +18.0 ^{MD}	7.9		
	³ H ₅	782	305.2 ^{ED} +74.4 ^{MD}	27.0		
	³ F ₄	651	108.4 ^{ED} +5.6 ^{MD}	8.1		
	³ H ₆	473	743.2 ^{ED}	52.8		
¹ D ₂	¹ G ₄	1438	195.0 ^{ED}	0.9	22610.8	0.044
	³ F ₂ + ³ F ₃	747	2399.3 ^{ED} +100.1 ^{MD}	11.0		
	³ H ₄	650	736.0 ^{ED}	3.2		
	³ H ₅	506	46.4 ^{ED}	0.3		
	³ F ₄	448	9022.0 ^{ED}	39.9		
	³ H ₆	356	10112.0 ^{ED}	44.7		

* $\langle\lambda\rangle$ - calculated mean emission wavelength, A_{Σ}^{calc} - probability of radiative spontaneous transitions (ED + MD), $B(JJ)$ - luminescence branching ratio, A_{tot} and τ_{rad} - total probability of radiative spontaneous transitions (ED+MD) and radiative lifetime of the excited state, respectively. ED and MD stand for electric-dipole and magnetic-dipole transitions, respectively.

Table 10. Comparison of the semi-experimental and theoretical integrated absorption cross sections* for the ${}^3\text{H}_4 \leftrightarrow {}^3\text{F}_4$ and ${}^3\text{H}_4 \leftrightarrow {}^3\text{H}_5$ transitions of Tm^{3+} ions in fluoride crystals.

Material	Transition	$S_{\text{calc}}^{\text{ED}}$ $\times 10^{20}$, cm^2	$S_{\text{calc}}^{\text{MD}}$ $\times 10^{20}$, cm^2	$\int \sigma_{\text{abs,calc}}(\lambda) d\lambda$ $\times 10^{20}$ $\text{cm}^2 \times \text{nm}$	Z_u/Z_l	λ_{ZL} , nm	$\int \langle \sigma_{\text{abs}} \rangle (\lambda) d\lambda$ $\times 10^{20}$, $\text{cm}^2 \times \text{nm}$
Tm:KY ₃ F ₁₀	${}^3\text{F}_4 \rightarrow {}^3\text{H}_4$	0.788	0.139	18.7	1.07	1443	22.9
	${}^3\text{H}_5 \rightarrow {}^3\text{H}_4$	0.767	0.245	27.8	1.22	2258	38.7
Tm:LiYF ₄	${}^3\text{F}_4 \rightarrow {}^3\text{H}_4$	0.705	0.139	17.4	1.56	1428	17.1
	${}^3\text{H}_5 \rightarrow {}^3\text{H}_4$	0.597	0.245	22.7	0.90	2317	29.0
Tm:LiLuF ₄	${}^3\text{F}_4 \rightarrow {}^3\text{H}_4$	0.752	0.147	18.5	1.61	1428	17.7
	${}^3\text{H}_5 \rightarrow {}^3\text{H}_4$	0.690	0.237	24.9	0.89	2320	24.1
Tm:BaY ₂ F ₈	${}^3\text{F}_4 \rightarrow {}^3\text{H}_4$	0.856	0.147	21.5	1.12	1431	16.7
	${}^3\text{H}_5 \rightarrow {}^3\text{H}_4$	1.173	0.237	39.7	1.07	2286	39.3

* $S_{\text{calc}}^{\text{ED}}$ and $S_{\text{calc}}^{\text{MD}}$ – ED and MD line strengths, respectively, $\int \sigma_{\text{abs,calc}}(\lambda) d\lambda$ – calculated integrated absorption cross-section according to Eq. (7), Z_u/Z_l – the ratio of partition functions, Eq. (6), λ_{ZL} – ZL wavelength, $\int \langle \sigma_{\text{abs}} \rangle (\lambda) d\lambda$ – polarization-averaged integrated absorption cross-section determined from the SE cross-sections with Eq. (5).